ELSEVIER

Advances in Water Resources 23 (2000) 699–723

Advances in Water Resources

www.elsevier.com/locate/advwatres

Numerical simulation of non-isothermal multiphase tracer transport in heterogeneous fractured porous media

Yu-Shu Wu *, Karsten Pruess

Earth Sciences Division, Lawrence Berkeley National Laboratory, Earth Sciences Division, MS 90-1116, One Cyclotron Road, Berkeley, CA 94720, USA

Received 17 June 1999; received in revised form 27 December 1999; accepted 19 January 2000

Abstract

We have developed a new numerical method for modeling tracer and radionuclide transport through heterogeneous fractured rocks in a non-isothermal multiphase system. The model formulation incorporates a full hydrodynamic dispersion tensor, based on three-dimensional velocity fields with a regular or irregular grid in a heterogeneous geological medium. Two different weighting schemes are proposed for spatial interpolation of three-dimensional velocity fields and concentration gradients to evaluate the mass flux by dispersion and diffusion of a tracer or radionuclide. The fracture–matrix interactions are handled using a dual-continua approach, such as the double- or multiple-porosity, or dual-permeability. This new method has been implemented into a multi-dimensional numerical code to simulate processes of tracer or radionuclide transport in non-isothermal, three-dimensional, multiphase, porous/fractured subsurface systems. We have verified this new transport-modeling approach by comparing its results to the analytical solution of a parallel-fracture transport problem. In addition, we use published laboratory results and the particle-tracking scheme to further validate the model. Finally, we present two examples of field applications to demonstrate the use of the proposed methodology for modeling tracer and radionuclide transport in unsaturated fractured rocks.

Keywords: Numerical reservoir simulation; Solute transport; Tracer and radionuclide transport; Multiphase flow and transport; Hydrodynamic dispersion; Fractured reservoir

1. Introduction

Flow and transport through fractured porous media, which occur in many subsurface systems, have received considerable increasing attention in recent years because of their importance in the areas of underground natural resource recovery, waste storage, soil physics, and environmental remediation. Since the 1960s, significant progress has been made in understanding and modeling fracture flow and transport phenomena in porous media [2,19,33,43]. Despite these advances, modeling the coupled processes of multiphase fluid flow, heat transfer, and chemical migration in a fractured porous medium remains a conceptual and mathematical challenge. The difficulty stems from the nature of inherent heterogeneity and uncertainties associated with fracture–matrix systems for any given field problem, as well as the computational intensity required. Numerical modeling approaches currently used for simulating these coupled processes are generally based on methodologies developed for petroleum and geothermal reservoir simulations. They involve solving fully coupled formulations describing these processes using finite-difference or finite-element schemes with a volume averaging approach.

Early research on flow and transport through fractured rocks was primarily related to the development of petroleum and geothermal reservoirs [19,31,51]. Later on, problems involving solute and contaminant transport in fractured aquifers were increasingly recognized in the groundwater literature, and several numerical approaches were developed [8,16,34]. Similar problems were encountered in soil science, which lead to the development of a "two-region" type model for studies of solute movement in aggregated field soils, or dual-continua media [15,41]. More recently, suitability evaluation of underground geological storage of high-level radioactive wastes in unsaturated fractured rocks has

* Corresponding author. Tel.: +1-510-486-7291; fax: +1-510-486-5686.

E-mail address: yswu@lbl.gov (Y.-S. Wu).

0309-1708/00/$ - see front matter
PII: S0309-1708(00)00008-7

Notation

A_{nm}	area between connected gridblocks n and m (m^2)
C_r	rock compressibility (1/Pa)
C_T	rock thermal expansion coefficient (1/°C)
C_{va}	air-specific heat at constant volume (J/kg °C)
D_n, D_m	distance from center of first (n) and second (m) element, respectively, to their common interface (m)
D_{nm}	distance between the centers of the two connected elements (m)
d_f, d_m	molecular diffusion coefficient (m^2/s) of a component in a fluid phase in fractures and matrix, respectively
$\underline{D}_\beta^\kappa$	diffusion–dispersion tensor accounting for both molecular diffusion and hydrodynamic dispersion for component κ in phase β (m^2/s)
$\underline{D}_{\beta,f}$	diffusion–dispersion tensor accounting for both molecular diffusion and hydrodynamic dispersion for a component in phase β in fractures, defined in Eq. (2.3.1) (m^2/s)
$\underline{D}_{\beta,fm}$	diffusion–dispersion tensor accounting for both molecular diffusion and hydrodynamic dispersion for a component in phase β in fracture–matrix or inner matrix–matrix connections, defined in Eq. (2.3.3) (m^2/s)
$\underline{D}_{\beta,m}$	diffusion–dispersion tensor accounting for both molecular diffusion and hydrodynamic dispersion for a component in phase β in matrix, defined in Eq. (2.3.2) (m^2/s)
$F_{A,nm}^{(\kappa)}$	components of advective mass flow of component κ along connection nm (kg/s m^2)
$F_{D,nm}^{(\kappa)}$	components of diffusive mass flow component κ along connection nm (kg/s m^2)
$F_{nm}^{(\kappa)}$	flow components of mass ($\kappa = 1$, 2 and 3) (kg/s m^2) or energy ($\kappa = 4$) (W/m^2) flow along connection nm
$F_{\beta,nm}$	flow components of mass of phase β along connection nm (kg/s m^2)
$\mathbf{F}_A^{(\kappa)}$	advective flux vector of component κ (kg/s m^2)
$\mathbf{F}_D^{(\kappa)}$	dispersive flux vector of component κ (kg/s m^2)
$\mathbf{F}^{(4)}$	heat flux vector (W/m^2)
$\boldsymbol{g}$	gravitational acceleration vector (m/s^2)
g_{nm}	component of the gravitational acceleration in the direction from m to n (m/s^2)
h_β	specific enthalpy of phase β (J/kg)
h_β^κ	specific enthalpy of component κ in phase β (J/kg)
k	absolute permeability of fractures or matrix (m^2)
K_d^κ	distribution coefficient of component κ between the water (liquid) phase and rock solids (m^3/kg)
K_H	Henry's constant (Pa)
K_P	equilibrium partitioning coefficient of a component between gas and liquid phases
$k_{r\beta}$	relative permeability to phase β
K_{th}	rock thermal conductivity (W/m °C)
M_κ	molecular weight of component κ
$M_n^{\kappa,k+1}$	accumulation terms for mass component ($\kappa = 1$, 2 and 3) (kg/ m^3) or energy ($\kappa = 4$) (J/m^3) of gridblock n at time level $k+1$.
M^κ	accumulation terms for mass component ($\kappa = 1$, 2 and 3) (kg/ m^3) or energy ($\kappa = 4$) (J/m^3) of gridblock n, defined in Eqs. (3.1.2)–(3.1.4)
$\mathbf{n}$	unit vector along the connection between two gridblocks n and m
n_i	directional cosine of the unit vector $\mathbf{n}$ ($i = x, y, z$)
nm	two connected elements or connection of n and m
P	pressure (Pa)
P^0	reference pressure (Pa)
P_c	gas–water capillary pressure (Pa)
P_β	pressure in phase β (Pa)
P_g^κ	saturated partial pressure of component κ in gas (Pa)
q^E	source/sink or fracture–matrix exchange terms for energy (W/m^3)
q^κ	source/sink or fracture–matrix exchange terms for component κ (kg/s m^3)
q_n^κ	source/sink or fracture–matrix exchange terms for component κ at element n (kg/s m^3)
R	universal gas constant (mJ/mol K)
$R_n^{\kappa,k+1}$	residual term of mass balance of component κ ($\kappa = 1$, 2 and 3) (kg/m^3) and energy (J/m^3) balance ($\kappa = 4$) at element n of time level $k+1$
S_β	saturation of phase β in fracture and matrix continua, respectively
$S_{\beta,f}$	saturation of phase β in fracture continuum
$S_{\beta,m}$	saturation of phase β in matrix continuum
t	time (s)
Δt	time step (s)

T	formation temperature (°C)
T_n	temperature at element n (°C)
T_m	temperature at element m (°C)
T^0	reference formation temperature (°C)
U_β	internal energy of phase β (J/kg)
U_s	internal energy of rock solids (J/kg)
U_g^w	internal energy of water vapor (J/kg)
V_n	volume of element n (m^3)
v_{nm}	Darcy's velocity component (m/s)
$v_{n,i}$	component of Darcy's velocity of a phase in the direction i ($i = x, y$ and z) at element n (m/s)
v_p	pore flow velocity (m/s)
$\mathbf{v}_n$	Darcy's velocity at element n (m/s)
$\mathbf{v}_\beta$	Darcy's velocity of phase β (m/s)
$\mathbf{v}_{\beta,f}$	Darcy's velocity of phase β in fractures (m/s)
$\mathbf{v}_{\beta,fm}$	Darcy's velocity of phase β between fractures and matrix or inner matrix–matrix (m/s)
$\mathbf{v}_{\beta,m}$	Darcy's velocity of phase β in matrix (m/s)
x_i	generic notation for the ith primary variable ($i = 1, 2, 3$ and 4)
$x_{i,p}$	generic notation for the ith primary variable at Newton iteration level p ($i = 1, 2, 3$ and 4)
X_L^t	mass fraction of tracer in the liquid phase
$X_n^{(\kappa)}$	mass fraction of component κ in a phase at element n
$X_\beta^{(\kappa)}$	mass fraction of component κ in phase β
$\nabla X^{(\kappa)}$	mass fraction gradient of component κ along connection nm
x, y, z	three Cartesian coordinates with z being in the vertical direction (m)

Greek symbols

$\alpha_{L,f}$	longitudinal dispersivity of fractures (m)
$\alpha_{L,m}$	longitudinal dispersivity of matrix (m)
$\alpha_{T,f}$	transverse dispersivity of fractures (m)
α_{fm}	longitudinal dispersivity along fracture–matrix or inner matrix–matrix connections (m)
δ_{ij}	Kronecker delta function ($\delta_{ij} = 1$ for $i = j$, and $\delta_{ij} = 0$ for $i \neq j$)
ϕ	effective porosity of fracture or matrix continua
ϕ_f	effective porosity of fracture continuum
ϕ_m	effective porosity of matrix continuum
ϕ^0	effective porosity of fracture or matrix continua at reference conditions
λ_κ	radioactive decay constant of the tracer/radionuclide (component $\kappa = 3$ only) (s^{-1})
μ_β	viscosity of fluid β (Pa s)
ρ_β	density of phase β at in situ conditions (kg/m^3)
$\rho_{\beta,nm}$	averaged density of phase β between element n and m (kg/m^3)
ρ_s	density of rock grains (kg/m^3)
ρ_g^κ	defined in Table 1 (kg/m^3)
τ_f, τ_m	tortuosity of matrix and fractures, respectively
ω_L^a	mole fraction of air in liquid phase

Subscripts

f	fracture
g	gas phase
i	index for primary variables or Cartesian coordinates
j	index for Cartesian coordinates
L	liquid phase
m	index of gridblocks of neighbors to n; or total number of connected elements to element n; or matrix
n	index of gridblocks
nm	between two connected gridblocks n and m, or appropriate averaging between two gridblocks
p	Newton iteration level
r	relative or rock
v	volume
x, y, z	x-, y-, and z-direction
β	index for fluid phase ($\beta =$ L for liquid and g for gas)

Superscripts

a	air component
E	energy
k	previous time step level
$k+1$	current time step level
t	tracer
w	water component
κ	index for mass components ($\kappa = 1$ or w for water, 2 or a for air, and 3 or t for tracer/radionuclide); and for energy ($\kappa = 4$)

generated a lot of interest in investigations of tracer or radionuclide transport in a non-isothermal, multiphase fluid fractured geological system [3]. In particular, the application of tracer tests, including environmental tracers and man-made tracer injection, has become an important technique in characterizing the fractured, unsaturated rocks at Yucca Mountain, a potential underground repository of radioactive wastes [4,36,53].

Even with the continual progress made in both computational algorithms and computer hardware in

the past few decades, simulating transport of a tracer or radionuclide in heterogeneous fractured porous media remains difficult with a numerical method. It becomes even more difficult when dealing with tracer transport in a multiphase and non-isothermal flow system using a general three-dimensional, irregular grid. One of the primary problems in solving advection–diffusion type transport equations in a complex geological medium is how to handle the diffusion/dispersion tensor in order to estimate accurately the dispersive terms of mass transport with including fracture–matrix interactions. Numerical modeling approaches in the literature generally use schemes that are based on regular grids and a partially implemented dispersion tensor. In most cases, these methods can handle only the transport problem under single-phase flow conditions. Very few studies have been conducted for modeling solute transport using a regular or irregular three-dimensional grid in multiphase, complex fractured geological systems with full implementation of the dispersion tensor [48].

Most numerical modeling approaches for solute transport in the literature [17,18,28] use numerical schemes that are based on regular grids with finite-element or finite-difference spatial discretization. For multiphase, non-isothermal flow and transport, a number of numerical models have been developed [5,6,9,12,23–25,27,40,52]. In addition, reactive transport of multi-species or radionuclides in a multiphase system has also been included in several models and studies [20,42,52]. However, these developed methodologies are most limited either to isothermal single-phase or to single-continuum medium conditions with regular grids. When dealing with non-isothermal, multiphase transport in fractured rocks, hydrodynamic dispersion effects are generally ignored [5,6,52]. Few investigations have addressed issues related to using fully-implemented dispersion tensors to modeling flow and transport processes in fractured rocks.

We have developed a new numerical method for modeling tracer or radionuclide transport in a non-isothermal multiphase system through heterogeneous fractured rocks. The model formulation incorporates a full hydrodynamic dispersion tensor, based on three-dimensional velocity fields using a regular or irregular grid in a heterogeneous geological system. Two different weighting schemes are presented for spatial interpolation of three-dimensional velocity fields and concentration gradients to evaluate the mass flux by dispersion and diffusion of a tracer or radionuclide. The proposed model formulation is applicable to both single-porosity porous media and fractured rocks. For transport in a fractured medium, fracture–matrix interactions are handled using a dual-continua approach, such as double- or multiple-porosity, or dual-permeability. This new method has been implemented into a multidimensional numerical code to simulate processes of tracer/radionuclide transport in non-isothermal, three-dimensional, multiphase, porous/fractured subsurface systems, using a regular or irregular, integral finite-difference grid.

In this paper, we discuss the model formulation, a complete set of constitutive relations, and the numerical schemes implemented. We give several examples in an effort to verify this new transport-modeling approach by comparing its results from analytical solutions, published laboratory tests, and other modeling approaches. Finally, two examples of field applications are presented to demonstrate the use of the proposed methodology for modeling transport in unsaturated fractured rocks.

2. Model formulation

The multiphase system under study consists of two phases, liquid (water) and gas, and they in turn consist of three mass components: air, water, and tracer (or radionuclide). Although both air and water are composed of several chemical components, they are here treated as single ''pseudo-components'' with averaged properties. To derive governing equations of fluid and heat flow, as well as tracer transport in the two-phase, three-component, non-isothermal system using a dual-continua conceptual model, we assume that a continuum approach is applied to both fractures and matrix, respectively, within a representative elementary volume (REV) in a fractured porous formation. Each REV contains enough fractures and matrix for such a continuum representation. The condition of local thermodynamic equilibrium is assumed so that temperatures, phase pressures, densities, viscosities, enthalpies, and component concentrations in either fractures or matrix domains are the same locally at any REV of the formation at any time. Darcy's law is used to describe flow of each fluid phase. A tracer is transported by advection and diffusion/dispersion, and heat is transferred by convection and conduction mechanisms. In addition, first-order decay is taken into account for the tracer and adsorption of a tracer on rock matrix and/or fractures is described by an equilibrium isotherm with a constant distribution coefficient.

2.1. Governing equations

In a dual-continua approach, processes of flow and transport in fractured rocks are described separately using a pair of governing equations for the fracture and matrix systems. This conceptualization results in a set of partial differential equations in the dual-continua formulation for flow and transport in fractured media, which are in the same form as that for a single-continuum porous medium [12,27,49].

The transport equation of each component κ within the fracture or matrix continuum of a REV can be written as follows:

$$\frac{\partial}{\partial t}\left\{\phi\sum_{\beta}\left(\rho_\beta S_\beta X_\beta^\kappa\right)+(1-\phi)\rho_{\rm s}\rho_{\rm L}X_{\rm L}^\kappa K_{\rm d}^\kappa\right\}+\lambda_\kappa\left\{\phi\sum_{\beta}\left(\rho_\beta S_\beta X_\beta^\kappa\right)+(1-\phi)\rho_{\rm s}\rho_{\rm L}X_{\rm L}^\kappa K_{\rm d}^\kappa\right\}=-\sum_{\beta}\nabla\cdot\left(\rho_\beta X_\beta^\kappa\mathbf{v}_\beta\right)+\sum_{\beta}\nabla\cdot\left(\rho_\beta\underline{D}_\beta^\kappa\cdot\nabla X_\beta^\kappa\right)+q^\kappa \tag{2.1.1}$$

and the energy conservation equation is

$$\frac{\partial}{\partial t}\left\{\sum_{\beta}\left(\phi\rho_\beta S_\beta U_\beta\right)+(1-\phi)\rho_{\rm s}U_{\rm s}\right\}=-\sum_{\beta}\nabla\cdot\left(h_\beta\rho_\beta\mathbf{v}_\beta\right)+\sum_{\beta}\sum_{\kappa}\nabla\cdot\left(\rho_\beta h_\beta^\kappa\underline{D}_\beta^\kappa\cdot\nabla X_\beta^\kappa\right)+\nabla\cdot\left(K_{\rm th}\nabla T\right)+q^{\rm E}, \tag{2.1.2}$$

where subscript β is an index for fluid phase ($\beta={\rm L}$ for liquid, and g for gas); κ an index for components ($\kappa=1$ or w for water, 2 or a for air, and 3 or t for tracer/radionuclide); q^κ and $q^{\rm E}$ are source/sink or fracture–matrix exchange terms for component κ and energy, respectively; and the rest of symbols and notations, in Eqs. (2.1.1) and (2.1.2) and those below, are defined in the table of Notation.

In Eqs. (2.1.1) and (2.1.2), $\mathbf{v}_\beta$ is the Darcy's velocity of phase β, defined as

$$\mathbf{v}_\beta=-\frac{kk_{{\rm r}\beta}}{\mu_\beta}(\nabla P_\beta-\rho_\beta\mathbf{g}) \tag{2.1.3}$$

for fluid flow of phase β of fracture and matrix continua, respectively.

2.2. Constitutive relations

The governing equations (2.1.1) and (2.1.2), mass and energy balance for fluids, heat and tracer, need to be supplemented with constitutive equations, which express all secondary variables and parameters as functions of a set of primary thermodynamic variables selected. For simplification in applications, it is assumed in the current model that the effects of tracer or radionuclide on thermodynamic properties of liquid and gas are negligible. In situations where a tracer or radionuclide is slightly soluble in liquid and/or in gas phase, such as in most laboratory and field tracer tests or radionuclide transport, this assumption provides very good approximations. Table 1 lists a complete set of the constitutive relationships used to complete the description of

Table 1
Constitutive relations and functional dependence

Definition of relations	Function
Fluid saturation	$S_{\rm L}+S_{\rm g}=1$
Mass fraction	$X_\beta^1+X_\beta^2+X_\beta^3=1$
Capillary pressure	$P_{\rm L}=P_{\rm g}-P_{\rm c}(S_{\rm L})$
Relative permeability	$k_{{\rm r}\beta}=k_{{\rm r}\beta}(S_{\rm L})$
Liquid density	$\rho_{\rm L}=\rho_{\rm L}(P,T)$
Gas density	$\rho_{\rm g}=\rho_{\rm g}^{\rm a}+\rho_{\rm g}^{\rm w}$ with $\rho_{\rm g}^{\rm a}=\frac{P_{\rm g}^{\rm a}M_{\rm a}}{RT}$, $\rho_{\rm g}^{\rm w}=\frac{P_{\rm g}^{\rm w}M_{\rm w}}{RT}$, and $P_{\rm g}^{\rm a}=P_{\rm g}-P_{\rm g}^{\rm w}$
Fluid viscosity	$\mu_\beta=\mu_\beta(P,T)$
Henry's law	$\omega_{\rm L}^{\rm a}=P_{\rm g}^{\rm a}/K_{\rm H}$
Air mass fraction in liquid phase	$X_{\rm L}^{\rm a}=\frac{\omega_{\rm L}^{\rm a}M_{\rm a}}{\omega_{\rm L}^{\rm a}M_{\rm a}+(1-\omega_{\rm L}^{\rm a})M_{\rm w}}$
Air mass fraction in gas phase	$X_{\rm g}^{\rm a}=\rho_{\rm g}^{\rm a}/\rho_{\rm g}$
Equilibrium partitioning	$X_{\rm g}^{\rm t}=K_{\rm P}X_{\rm L}^{\rm t}$
Partitioning coefficient	$K_{\rm P}=K_{\rm P}(P,T)$
Specific enthalpy of liquid water	$h_{\rm L}=U_{\rm L}+P_{\rm L}/\rho_{\rm L}$
Specific enthalpies of air	$h_{\rm g}^{\rm a}=C_{\rm va}T+P_{\rm g}^{\rm a}/\rho_{\rm g}^{\rm a}$
Specific enthalpies of water vapor	$h_{\rm g}^{\rm w}=U_{\rm g}^{\rm w}+P_{\rm g}^{\rm w}/\rho_{\rm g}^{\rm w}$
Gas phase specific enthalpy	$h_{\rm g}=X_{\rm g}^{\rm a}h_{\rm g}^{\rm a}+X_{\rm g}^{\rm w}h_{\rm g}^{\rm w}$
Thermal conductivity of the media	$K_{\rm th}=K_{\rm th}(S_{\rm L})$
Porosity	$\phi=\phi^0(1+C_{\rm r}(P-P^0)-C_T(T-T^0))$

multiphase flow and tracer transport through fractured porous media in this study.

2.3. Hydrodynamic dispersion tensor

Under the conceptualization of a dual-continua approach, three types of flow need to be considered in evaluating dispersion coefficients. They are:
1. global fracture–fracture flow,
2. global matrix–matrix flow, and
3. local fracture–matrix or matrix–matrix interaction.

We assume that hydrodynamic dispersion associated with global flow through fracture or matrix systems is described by a general dispersion model [35] for fracture and matrix systems separately. For transport in fractures

$$\underline{D}_{\beta,\mathrm{f}} = \alpha_{\mathrm{T,f}}|\mathbf{v}_{\beta,\mathrm{f}}|\delta_{ij} + (\alpha_{\mathrm{L,f}} - \alpha_{\mathrm{T,f}})\frac{\mathbf{v}_{\beta,\mathrm{f}}\mathbf{v}_{\beta,\mathrm{f}}}{|\mathbf{v}_{\beta,\mathrm{f}}|} + \phi_{\mathrm{f}} S_{\beta,\mathrm{f}} \tau_{\mathrm{f}} d_{\mathrm{f}} \delta_{ij} \tag{2.3.1}$$

for transport in matrix

$$\underline{D}_{\beta,\mathrm{m}} = \alpha_{\mathrm{T,m}}|\mathbf{v}_{\beta,\mathrm{m}}|\delta_{ij} + (\alpha_{\mathrm{L,m}} - \alpha_{\mathrm{T,m}})\frac{\mathbf{v}_{\beta,\mathrm{m}}\mathbf{v}_{\beta,\mathrm{m}}}{|\mathbf{v}_{\beta,\mathrm{m}}|} + \phi_{\mathrm{m}} S_{\beta,\mathrm{m}} \tau_{\mathrm{m}} d_{\mathrm{m}} \delta_{ij}. \tag{2.3.2}$$

If global matrix–matrix flow and transport are taken into account, e.g., in a dual-permeability conceptualization.

For diffusive transport processes between fractures and matrix or inside matrix, we introduce a new relation

$$\underline{D}_{\beta,\mathrm{fm}} = \alpha_{\mathrm{fm}}|\mathbf{v}_{\beta,\mathrm{fm}}| + \phi_{\mathrm{m}} S_{\beta,\mathrm{m}} \tau_{\mathrm{m}} d_{\mathrm{m}}. \tag{2.3.3}$$

In Eqs. (2.3.1)–(2.3.3), $\underline{D}_{\beta,\mathrm{f}}$, $\underline{D}_{\beta,\mathrm{m}}$, and $\underline{D}_{\beta,\mathrm{fm}}$ are combined diffusion–dispersion tensors for transport through fractures, matrix, and between fractures and matrix or inside matrix, repectively; $\alpha_{\mathrm{T,f}}$, $\alpha_{\mathrm{T,m}}$, $\alpha_{\mathrm{L,f}}$, and $\alpha_{\mathrm{L,m}}$ are transverse and longitudinal dispersivities, respectively, of fractures and matrix; and α_{fm} is longitudinal dispersivity along fracture–matrix or inner matrix–matrix connections.

3. Numerical scheme

3.1. Discrete equations

The numerical implementation of the tracer transport model discussed above is based on the framework of the TOUGH2 code [29,30] and the model formulation has been incorporated into a general purpose, two-phase fluid and heat flow, tracer-transport reservoir simulator, T2R3D [47,48]. The component mass and energy balance Eqs. (2.1.1) and (2.1.2) are discretized in space using the integral finite-difference method [22] in a porous and/or fractured medium. The discretization and definition of the geometric variables are illustrated in Fig. 1. The time discretization is carried out with a backward, first-order, finite-difference scheme. The discrete non-linear equations for water, air, tracer/radionuclide, and heat at gridblock n can be written as follows [49]:

$$R_{\mathrm{n}}^{\kappa,k+1} = M_{\mathrm{n}}^{\kappa,k+1}(1+\lambda_\kappa \Delta t) - M_{\mathrm{n}}^{\kappa,k} - \frac{\Delta t}{V_{\mathrm{n}}}\left\{\sum_{\mathrm{m}}\left(A_{\mathrm{nm}}F_{\mathrm{nm}}^{(\kappa),k+1}\right) + V_{\mathrm{n}} q_{\mathrm{n}}^{\kappa,k+1}\right\} \quad (\kappa = 1,\ 2,\ 3,\ \text{and } 4), \tag{3.1.1}$$

where superscript κ is an equation index, and $\kappa = 1,\ 2,\ 3$, and 4 denote water, air, tracer/radionuclide and heat equations, respectively; superscript k denotes the previous time level; $k+1$ the current time level; V_{n} the volume of element n (matrix or fractured block); Δt is time step size; m is a neighbor element, to which element n is directly connected. Subscripts n and nm denote element n and connection between elements n and m. M is a volume-normalized extensive quantity, or accumulation term of mass or energy; and M_{n} is the average value of M over element volume, V_{n}; F_{nm} is the average value of the (inward) normal component mass or heat fluxes, over the surface segment area, A_{nm}, between volume elements V_{n} and V_{m}. The decay constants, λ_κ, are 0 unless $\kappa = 3$ for a decaying tracer/radionuclide component.

The accumulation terms for water and air components in (3.1.1) are evaluated as

$$M^\kappa = \sum_\beta \left(\phi S_\beta \rho_\beta X_\beta^\kappa\right) \quad (\kappa = 1 \text{ and } 2) \tag{3.1.2}$$

for tracer ($\kappa = 3$),

$$M^3 = \sum_\beta \left(\phi S_\beta \rho_\beta X_\beta^3\right) + (1-\phi)\rho_{\mathrm{s}}\rho_{\mathrm{L}} X_{\mathrm{L}}^3 K_{\mathrm{d}}^3 \tag{3.1.3}$$

and for thermal energy ($\kappa = 4$),

$$M^4 = \sum_\beta (\phi \rho_\beta S_\beta U_\beta) + (1-\phi)\rho_{\mathrm{s}} U_{\mathrm{s}}. \tag{3.1.4}$$

The discretized fluxes are expressed in terms of parameters averaged between elements V_{n} and V_{m}. The net mass flux of diffusion and dispersion of a component along the connection of elements V_{n} and V_{m} is determined by

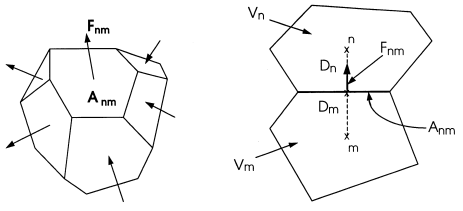

Fig. 1. Space discretization and geometry data in the integral finite-difference method [29].

$$F_{nm}^{(\kappa)} = \mathbf{n} \cdot \left(\mathbf{F}_D^{(\kappa)} + \mathbf{F}_A^{(\kappa)} \right) \quad (\kappa = 1,\ 2 \text{ and } 3), \tag{3.1.5}$$

where $\mathbf{n}$ is the unit vector at the connection between the two blocks of n and m along connection nm, with a component n_i $(i = x, y, z)$, or directional cosines, in the x-, y-, or z- direction, respectively; $\mathbf{F}_D^{(\kappa)}$ and $\mathbf{F}_A^{(\kappa)}$ are dispersive and advective flux vectors, respectively, with

$$\mathbf{F}_D^{(\kappa)} = -\sum_\beta \left(\rho_\beta \underline{D}_\beta^\kappa \cdot \nabla X_\beta^\kappa \right) \tag{3.1.6}$$

and

$$\mathbf{F}_A^{(\kappa)} = \sum_\beta \left(X_\beta^{(\kappa)} \rho_\beta \mathbf{v}_\beta \right). \tag{3.1.7}$$

The heat flux vector is given by

$$\mathbf{F}^{(4)} = \sum_\beta (h_\beta \rho_\beta \mathbf{v}_\beta) - \sum_\beta \sum_\kappa \left(\rho_\beta h_\beta^\kappa \underline{D}_\beta^\kappa \cdot \nabla X_\beta^\kappa \right) - \nabla \cdot (K_{th} \nabla T). \tag{3.1.8}$$

Evaluation of components of the dispersive and advective flux vectors along the connection nm will be discussed in Sections 3.2 and 3.3.

Newton iteration is used to solve the non-linear, discrete Eq. (3.1.1), leading to a set of linear equations for the increments $(x_{i,p+1} - x_{i,p})$:

$$\sum_i \left[\frac{\partial R_n^{\kappa,k+1}}{\partial x_i} \right]_p (x_{i,p+1} - x_{i,p}) = -R_n^{\kappa,k+1}(x_{i,p}) \quad (i, \kappa = 1, 2, 3, 4 \text{ and } n = 1, 2, 3, \ldots, N), \tag{3.1.9}$$

where p is a Newton iteration index. In setting up (3.1.9), all terms in the Jacobian matrix are evaluated by numerical differentiation; x_i the ith primary variables selected; and N is the total number of elements in the grid. Eq. (3.1.9) represents a system of $4 \times N$ linearized equations, which is solved by an iterative sparse matrix solver [13]. Iteration is continued until the residuals $R_n^{\kappa,k+1}$ are reduced below a preset convergence tolerance.

We have developed several modules of the tracer-transport model, including a fully coupled formulation for liquid tracer and gas tracer transport coupled with fluid and heat flow, and a decoupled module, in which the fluid flow and temperature fields are predetermined and used as input parameters for transport calculations. The decoupled module is specifically designed for a situation in which fluid and temperature fields are at steady-state and can be predetermined by flow simulations only for fluids and heat. For the fully coupled formulation, there are four equations or four primary variables to be solved per gridblock and there is only one equation or one primary variable for the decoupled scheme.

For coupled or decoupled modules, the same form of equations, Eq. (3.1.9), need to be solved and for both cases the Newton iteration scheme is used. As in the TOUGH2 code [29], using an unstructured grid is inherent for the current model, i.e., the model always handles regular or irregular grids as unstructured grids. Therefore, the sparse matrix structure of the Jacobian is determined solely by the information on connections of a grid, supplied to the code, which is treated completely independent of regularity of a grid. In general, a variable switching scheme is needed in order to be able to evaluate residual terms each iteration using primary variables under various fluid conditions in assembly of the Jacobian matrix for a Newton. The selection of primary variables depend on the phase conditions, as well as whether a liquid or gas tracer is studied. The variable switching procedure affects the updating for secondary-dependent variables but does not affect the equation setup, because the equations are still mass- and energy-conservation equations for each block. Table 2 lists the selection of the primary variables used for evaluating the Jacobian matrix and residuals of the linear equation system and to be solved during iteration.

3.2. Dispersion tensor and diffusive flux

One of the key issues in developing the current tracer-transport model is how to implement the general, three-dimensional dispersion tensor of (2.3.1)–(2.3.3) using a regular or irregular grid, with the integral finite-difference discretization. We have to deal with the two problems:

1. how to average velocity fields for estimating a full dispersion tensor, and
2. how to determine the vector of concentration gradients.

Table 2
Choice and switching of primary variables

Module	Phase	Primary variables				
		x_1	x_2	x_3 [a]		x_4
				Liquid tracer	Gas tracer	
Fully coupled	Two-phase water and gas	P_g	$S_g + 10$	X_L^t	X_g^t	T
	Single-phase water	P_L	X_L^a	X_L^t	X_L^t	T
	Single-phase gas	P_g	X_g^a	X_g^t	X_g^t	T
Decoupled	Two-phase or single-phase water	X_L^t				

[a] Dependent on whether a liquid or gas tracer is simulated.

The following two new schemes are proposed and used in this study.

3.2.1. Velocity averaging scheme

To evaluate a full dispersion tensor, using Eqs. (2.3.1)–(2.3.3), what we need first is to estimate a velocity vector with respect to the global coordinates selected. When using a conventional finite-difference or finite-element discretization with irregular grids, however, only velocities, which are well defined at each Newton iteration or time step, are those relative to the local coordinates, for each gridblock, are to be used along connection lines between a block and its neighbors. Therefore, we need to convert local velocities along connections in the local coordinate system (Fig. 1) to a velocity vector, $\mathbf{v}_n$, in the system of global coordinates (x, y, z) at the block center for each block (n) of the grid. The averaging or weighting scheme used is a physically based method, called "projected area weighting method" [48,49]. In this method a global fracture or matrix velocity component, $\mathbf{v}_{n,i}$, of the vector $\mathbf{v}_n$ at the center of gridblock n is determined by the vectorial summation of the components of all local connection vectors in the same direction, weighted by the projected area in that direction as

$$\boldsymbol{v}_{n,i} = \frac{\sum_m (A_{nm}|n_i|)(v_{nm}n_i)}{\sum_m (A_{nm}|n_i|)} \quad (i = x, y, z), \tag{3.2.1}$$

where m is the total number of connections between element V_n and all its neighboring elements V_m; and v_{nm} is the Darcy's velocity along connection nm in the local coordinate system. In this equation, the term $(A_{nm}|n_i|)$ is the projected area of the interface A_{nm} on to direction i of the global coordinate system, and $(v_{nm}n_i)$ gives the velocity component in direction i of the global coordinate system. Also, it should be mentioned that the absolute value for the directional cosines, n_i, is used for evaluating the projected area in Eq. (3.2.1), because only the positive areal values are needed in the weighting scheme.

Physically, flow along a connection of two gridblocks may be regarded as an individual velocity vector and can always be decomposed uniquely into three components along three orthogonal directions (x, y, z) in the global coordinates. To obtain a velocity vector at a gridblock center in the global coordinate system, one need to add all components of flow along every connection into and from the block, i.e., include all contributions to the same directions, projected from all connections to the block. In addition, a proper weighting scheme over velocity components from different connections is needed to account for the fact that a resultant velocity would be doubled, without weighting, when adding inflow and outflow vectors together under steady-state conditions. These arguments form the basis of Eq. (3.2.1). It is easy to show that a one-dimensional steady-state flow field in a three-dimensional domain is preserved exactly by Eq. (3.2.1), if a regular, cube-type grid is used with the one-dimensional flow direction being in coincident with a coordinate direction. In addition, the projected area-weighting scheme enforces the condition that flow crossing a larger connection area has more weight in the resultant velocity vector.

Once a velocity field is determined at each block center, we use a spatially harmonic weighting scheme to evaluate a velocity vector at the interfaces between element blocks, as illustrated in Fig. 2. In this figure, $\mathbf{v}_m$ and $\mathbf{v}_n$ are the fluid velocities at the center of each block, whereas $\mathbf{v}$ is the velocity of the fluid at the interface between blocks V_n and V_m. The positive direction of $\mathbf{n}$ is defined as the direction from the block center of V_m toward the block center of V_n, as shown in Fig. 2.

The velocity vector $\mathbf{v}$ at the interface of elements n and m is evaluated by harmonic weighting by the distances to the interface, using the velocities at the block centers of the two elements,

$$\frac{D_n + D_m}{v_i} = \frac{D_n}{v_{n,i}} + \frac{D_m}{v_{m,i}} \quad (i = x, y, z) \tag{3.2.2}$$

for its component v_i. Harmonic weighting is used because it preserves total transit time for solute transport along the connection.

3.2.2. Concentration gradient averaging scheme

The concentration or mass fraction gradient of the tracer/radionuclide is evaluated at the interface between gridblocks n and m as

$$\nabla X^{(\kappa)} = \left(\mathbf{n}_x \Delta X^{(\kappa)}_{nm}, \mathbf{n}_y \Delta X^{(\kappa)}_{nm}, \mathbf{n}_z \Delta X^{(\kappa)}_{nm}\right) \tag{3.2.3}$$

with

$$\Delta X^{(\kappa)}_{nm} = \frac{X^{(\kappa)}_m - X^{(\kappa)}_n}{D_m + D_n}. \tag{3.2.4}$$

Eq. (3.2.3) will be used to calculate the total diffusive and dispersive mass flux of a tracer/radionuclide along the connection of the two elements.

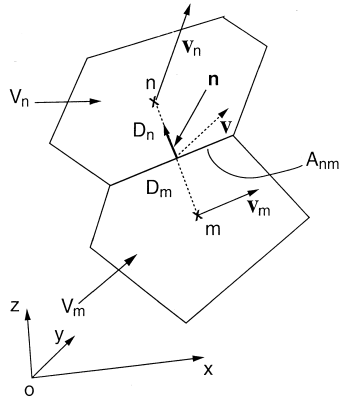

Fig. 2. Schematic of spatial averaging scheme for velocity fields in the integral finite difference method.

We have experimented with some other weighting schemes for averaging concentration gradients, such as using a fully three-dimensional vector, obtained similarly to averaging velocities discussed above. Numerical tests and comparisons with analytical solutions in multidimensional transport simulations indicate that use of Eqs. (3.2.3) and (3.2.4) gives the most accurate results.

3.2.3. Dispersive flux

The velocity $\mathbf{v}$ or $\mathbf{v}_\beta$, determined by Eqs. (3.2.1) and (3.2.2), is used in Eqs. (2.3.1) and (2.3.2) to evaluate the dispersion tensor of fractures or matrix, respectively, along the connection of the two elements. For transport between fractures and matrix, or inside matrix, the flow is usually approximated as one-dimensional linear, radial, or spherical, and the local velocities can be used directly in Eq. (2.3.3) to calculate the dispersion coefficients.

The net mass dispersive flux of diffusion and dispersion of a tracer/radionuclide along the connection of elements V_n and V_m is then determined by

$$F^{(\kappa)}_{D,nm} = \mathbf{n}\cdot\mathbf{F}^{(\kappa)}_D = -\mathbf{n}\cdot\left[\rho_\beta \underline{D}^\kappa_\beta \cdot \nabla X^{(\kappa)}_\beta\right]. \tag{3.2.5}$$

This diffusive flux is substituted into Eqs. (3.1.6) and (3.1.5) and then (3.1.1). It should be mentioned that Eq. (3.2.5) incorporates all contributions of both diagonal and off-diagonal terms, contributed by a full dispersion tensor, to dispersive fluxes and no negligence or approximation is made to any terms.

In calculating dispersive fluxes along a connection to a gridblock using Eq. (3.2.5), the vector of mass fraction gradients should be evaluated at every Newton iteration. However, the averaged velocity field for estimating the dispersion tensor may be updated at a time step level instead of an iteration level to save simulation time. This is equivalent to using an explicit scheme for handling dispersion coefficients, i.e., estimating dispersion coefficients using velocities at the beginning rather than at the end of a time step, as required by a full implicit method. A series of numerical tests indicate that this method is efficient and accurate, and no numerical difficulties have been encountered.

3.3. Advective fluid flux and heat flow

The mass fluxes of phase β along the connection nm is given by a discrete version of Darcy's law

$$F_{\beta,nm} = \rho_\beta \mathbf{v}_\beta = -\left\{k_{nm}\left[\frac{k_{r\beta}\rho_\beta}{\mu_\beta}\right]_{nm}\left[\frac{P_{\beta,m}-P_{\beta,n}}{D_{nm}} - \rho_{\beta,nm} g_{nm}\right]\right\}, \tag{3.3.1}$$

where the subscripts (nm) denote a suitable averaging at the interface between gridblocks n and m (interpolation, harmonic weighting, upstream weighting, etc.). D_{nm} the distance between the nodal points n and m, and g_{nm} is the component of gravitational acceleration in the direction from m to n. Then the advective flux of component κ of Eq. (3.1.7) is

$$F^{(\kappa)}_{A,nm} = \sum_\beta \left(X^k_\beta\right)_{nm} F_{\beta,nm}. \tag{3.3.2}$$

The total heat flux along the connection nm includes advective, diffusive, and conductive terms and is evaluated by

$$\mathbf{F}^{(4)}_{nm} = \sum_\beta [(h_\beta)_{nm} F_{\beta,nm}] - \sum_\beta \sum_\kappa \left\{\left(h^\kappa_\beta\right)_{nm} F^\kappa_{D,nm}\right\} - (K_{th})_{nm}\left[\frac{T_m - T_n}{D_{nm}}\right]. \tag{3.3.3}$$

It should be mentioned that only dispersive heat fluxes in the gas phase are included in the calculation, and they are ignored in the liquid phase.

Eqs. (3.2.5)–(3.3.3) are proposed to evaluate dispersive/advective mass transport and heat transfer terms for (3.1.1). In general they can be applied not only to global fracture–fracture or matrix–matrix connections between neighboring gridblocks, but also to determining fracture–matrix exchange terms, q^κ and q^E, for component κ and energy, respectively. When used for fracture–matrix interactions, a proper weighting scheme for flow, transport and heat transfer properties is needed (see Sections 3.4 and 3.6 below).

3.4. Fractured media

The technique used in the current model for handling flow and transport through fractured rock follows the dual-continua methodology [29,31,43]. The method treats fracture and rock matrix flow and interactions using a multicontinua numerical approach, including the double- or multiporosity method [51]; the dual-permeability method; and the more general "multiple-interacting continua" (MINC) method [31].

The classical double-porosity concept for modeling flow in fractured, porous media was developed by Warren and Root [43]. In this method, a flow domain is composed of matrix blocks of low permeability, embedded in a network of interconnected fractures. Global flow and transport in the formation occurs only through the fracture system, which is described as an effective porous continuum. The matrix behaves as spatially distributed sinks or sources to the fracture system without accounting for global matrix–matrix flow. The double-porosity model accounts for fracture–matrix interflow, based on a quasi-steady-state assumption.

The more rigorous method of MINC [31,33] describes gradients of pressures, temperatures and concentrations

between fractures and matrix by appropriate subgridding of the matrix blocks. This approach provides a better approximation for transient fracture–matrix interactions than using the quasi-steady-state flow assumption of the Warren and Root model. The basic concept of MINC is based on the assumption that changes in fluid pressures, temperatures and concentrations will propagate rapidly through the fracture system, while only slowly invading the tight matrix blocks. Therefore, changes in matrix conditions will be controlled locally by the distance to the fractures. Fluid flow and transport from the fractures into the matrix blocks can then be modeled by means of one- or multidimensional strings of nested gridblocks. In general, matrix–matrix connections can also be described by the MINC methodology.

As a special case of the MINC concept, the dual-permeability model considers global flow occurring not only between fractures but also between matrix gridblocks. In this approach, fracture and matrix are each represented by one gridblock, and they are connected to each other. Because of the one-block representation of fractures or matrix, the interflow between fractures and matrix has to be handled using some quasi-steady-state flow assumption, as used with the Warren and Root model. Also, because the matrix is approximated using a single gridblock, accuracy in evaluating gradients of pressures, capillary pressures, temperatures and concentrations within matrix may be limited. Under steady-state flow conditions, however, the gradients near the matrix surfaces become minimal, and the model is expected to produce accurate solutions.

The model formulation of this work, as discussed above, is applicable to both single-continuum and multicontinua media. When handling flow and transport through a fractured rock, a large portion of the work consists of generating a mesh that represents both fracture and matrix system. This fracture–matrix mesh is usually based on a primary, single-porous medium mesh, which is generated using only geometric information of the formation. Within a certain reservoir subdomain (corresponding to one finite-difference gridblock of the primary mesh), all fractures will be lumped into fractured continuum #1. All matrix material within a certain distance from the fractures will be lumped into one or several different matrix continua, as required by the double-porosity, dual-permeability, or MINC approximations. Several matrix subgridding schemes exist for designing different meshes for different fracture–matrix conceptual models [32].

Once a proper mesh of a fracture–matrix system is generated, fracture and matrix blocks are specified to represent fracture or matrix domains, separately. Formally they are treated exactly the same during the solution in the model. However, physically consistent fracture and matrix properties and modeling conditions must be appropriately specified for fracture and matrix systems, respectively.

3.5. Initial and boundary conditions

The initial status of a reservoir system needs to be specified by assigning a complete set of primary thermodynamic variables to each gridblock. A commonly used procedure for specifying a capillary-gravity equilibrium, tracer-free initial condition is using a restart option, in which a complete set of initial conditions is produced in a previous simulation with proper boundary conditions described.

First-type or Dirichlet boundary conditions denote constant or time-dependent phase pressure, saturation, temperature and concentration conditions. These types of boundary conditions can be treated using the big-volume method, in which a constant pressure/saturation node is specified with a huge volume while keeping all the other geometric properties of the mesh unchanged. However, caution should be taken on:

1. identifying phase conditions when specifying the "initial condition" for the big-volume boundary node, and
2. distinguishing upstream/injection from downstream/production nodes.

For a downstream node, diffusion and dispersion coefficients could be set to 0 to turn off unphysical diffusive fluxes, which may occur as a result of large concentration gradients. Once specified, primary variables will be fixed at the big-volume boundary nodes, and the code handles these boundary nodes exactly like any other computational nodes.

Flux-type or Neuman boundary conditions are treated as sink/source terms, depending on the pumping (production) or injection condition, which can be directly added to Eq. (3.1.1). This treatment of flux-type boundary conditions is especially useful for a situation where flux distribution along the boundary is known, such as dealing with surface infiltration. This method may also be used for an injection or pumping well connected to a single gridblock without injection or pumping pressures to be estimated. More general treatment of multilayered well boundary conditions is discussed in [46].

3.6. Weighting scheme

The proper spatial weighting scheme for averaging flow and transport properties in a highly heterogeneous formation is much debated in the literature. Traditionally in the petroleum literature, upstream weighting is used for relative permeabilities and harmonic weighting is used for absolute permeabilities in handling multiphase flow in heterogeneous porous media [1]. This technique works reasonably well for cases of multiphase

flow as long as the contrasts in flow properties of adjacent formation layers are not very large, such as in single-porosity oil reservoirs. For simulating multiphase flow in for highly heterogeneous fractured porous media, this traditional harmonic weighting scheme for absolute permeabilities may not applicable [39].

Selection of a weighting scheme becomes more critical when dealing with the coupled processes of multiphase flow, tracer transport, and heat transfer in a fractured medium, because often fracture and matrix characteristics greatly differ, with many orders of magnitude contrast of flow and transport properties, such as permeability and dispersivity. In recent years, more attention has been paid to weighting methods of flow and transport properties in the community of groundwater and unsaturated zone modeling. It has been found that upstream weighted relative permeability will result not only in physically consistent solutions, but also mathematical unconditional monotone, total variation diminishing conditions [11] for modeling unsaturated flow using a finite-volume discretization, such as the integral finite-difference approach used in this study. Other weighting schemes, such as central weightings, may converge to the incorrect, unphysical solution [10].

In addition to the weighting scheme for evaluating multiphase flow, we also need to select proper weighting techniques for calculating dispersive and advective transport, as well as heat flow. Recent work has shown that using high-order differencing or flux limiter schemes is very promising and efficient in reducing numerical dispersion effects [9,23] in a dissolved solute plume. For dispersive flux, certain averaging of diffusion–dispersion coefficients is also needed to resolve diffusive flux across gridblocks with step-change phase saturations. For example, a harmonic-weighted phase saturation is used as a weighting function for diffusion coefficients [12].

We have examined and tested various weighting schemes for fluid/heat flow and tracer transport through fractured rocks, and have found that there are no generally applicable weighting schemes that can be used to all problems. Selection of proper weighting schemes is in general problem or specific system-dependent. The weighting schemes used are:

1. upstream weighting for relative permeability for any connections;
2. harmonic or upstream weighting for absolute permeabilities for global fracture or matrix flow;
3. using matrix absolute permeability, thermal conductivity, molecular diffusion coefficients for fracture–matrix interactions;
4. phase saturation-based weighting functions for determining diffusion coefficients;
5. upstream weighted enthalpies for advective heat flow;
6. central weighted scheme for thermal conductivities of global heat conduction.

4. Verification and validation examples

Three examples are given in this section to provide verification of the numerical schemes of this work in handling transport in a multidimensional domain with hydrodynamic dispersion and molecular diffusion effects. Analytical solutions, laboratory results, and a particle-tracking scheme are used for the comparisons. The sample problems include:

- Tracer transport in a parallel-fracture system.
- Laboratory investigation of tracer transport through stratified porous media.
- Three-dimensional tracer transport using an unstructured grid.

4.1. Transport in a parallel-fracture system

This problem is used to verify the new scheme for estimating dispersion tensors in fractured porous rocks using a dual-continua approach. An analytical solution for contaminant transport through parallel fractures is available in the literature [38] to examine numerical solutions. The test problem concerns a two-dimensional, parallel-fracture system, with a saturated fracture–matrix unit of 10 m length, as illustrated in Fig. 3. The aperture of the fracture is 10^{-4} m, fracture spacing is 0.1 m, and the flow field is at steady-state with 0.1 m/day velocity along the fracture. A radionuclide is introduced at the inlet ($x = 0$) with a constant concentration, and transport occurs by advection, hydrodynamic dispersion, molecular diffusion, and decay.

The numerical solution of this problem is performed by the decoupled version of the model. In both flow and transport simulations, a one-dimensional, uniform linear grid of 100 elements was generated along the fracture, and a MINC mesh was made with nine subdivisions (one fracture element corresponding to eight matrix elements, laterally connecting to the fracture elements). The rest of the properties used in the comparison are listed in Table 3.

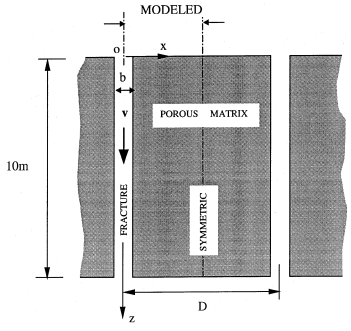

Fig. 3. Schematic of a parallel fracture-matrix system and modeled domain.

Table 3
Parameters used in the transport problem in a parallel fracture system

Fracture spacing	$D = 0.1$ m
Fracture aperture	$b = 1.0 \times 10^{-4}$ m
Fracture porosity	$\phi_f = 1.0$
Matrix porosity	$\phi_m = 0.1$
Molecular diffusion coefficient	$D_m = 1.0 \times 10^{-10}$ m^2/s
Fracture longitudinal, transverse dispersivity	$\alpha_{L,f} = 0.1$ m, $\alpha_{T,f} = 0.0$
Matrix longitudinal, transverse dispersivity	$\alpha_{L,m} = 0.0$, $\alpha_{T,m} = 0.0$
Fracture–matrix dispersivity	$\alpha_{fm} = 0.0$
Fracture, matrix tortuosities	$\tau_f = 1$, $\tau_m = 1$
Fracture pore velocity	$v_{p,f} = 0.1$ m/day
Temperature	$T = 25$°C
Downstream pressure	$P_L = 1.0 \times 10^5$ Pa
Source concentration	$C^{\text{radionuclide}} = 1.0$
Grid spacing	$\Delta x = \Delta y = 0.1$ m
Distribution coefficient in fractures	$K_{d,f} = 0.0$
Distribution coefficient in matrix	$K_{d,f} = 6.313 \times 10^{-6}$ m^3/kg
Radioactive decay constant	$\lambda = 8.0 \times 10^{-9}$ s^{-1}

A comparison of the normalized radionuclide concentrations along the fracture from the numerical solution and the analytical solution is shown in Fig. 4 for $t = 10$, 100, 300 and 500 days, respectively. The figure indicates that the simulated concentration profiles in fractures are in excellent agreement with the analytical solution in all cases.

4.2. Comparison with laboratory testing results

Sudicky et al. [37] presented an experimental investigation on the migration of a non-reactive solute in layered porous media under controlled laboratory conditions by injecting a tracer into a thin sand layer bounded by silt layers. This stratified, heterogeneous aquifer model can be conceptualized as a dual-continua medium with the highly permeable sand layer as "fracture" and the silt portion as "matrix", because a four-order-of-magnitude difference exists in permeabilities of the two media. We use their experimental results to benchmark our numerical scheme in handling solute transport through fractured rocks.

The laboratory model consists of a plexiglass box with internal dimensions of 1.0 m in length, 0.2 m in thickness, 0.1 m in width (a third dimension), as shown in Fig. 5. A layer of sand 0.03 m thick is situated between two layers of silt, each 0.085 m thick. The influent and effluent end caps, through which the displacing liquid containing a chloride tracer enters and leaves the sand layer, are screened over the sand layer only. A sodium chloride solution containing 100 mg/l Cl^- was used as the liquid tracer. Two breakthrough experiments were performed with different flow velocities in the sand

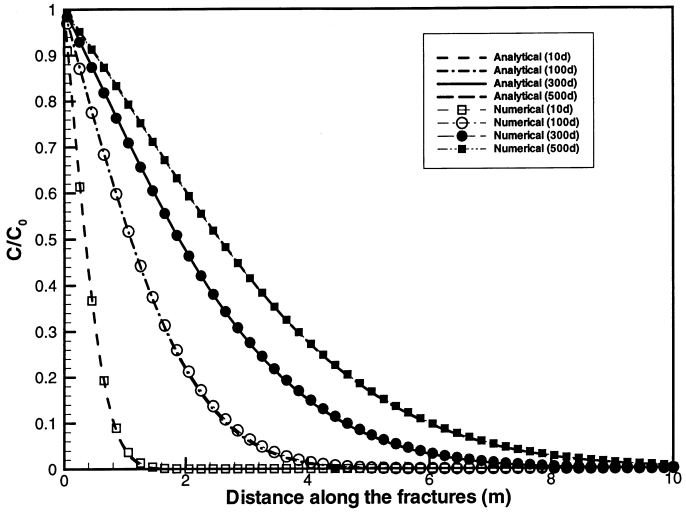

Fig. 4. Comparison of the normalized radionuclide concentrations along the fracture, simulated using numerical and analytical solutions.

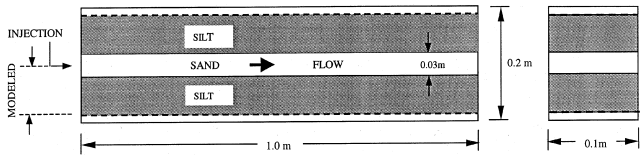

Fig. 5. Laboratory model [37] and modeled domain.

and different solute source conditions. Here we select the second, higher pore-velocity test, in which the pore velocity through the sand was kept at 0.5 m/day for 7 days, and then the influent solution was switched to a tracer-free solution under the ambient temperature 25°C.

This test is analyzed using a dual-continua approach in an effort to examine the numerical scheme for handling transport processes through fractured porous media with molecular diffusion, hydrodynamic dispersion, and advection. Due to the symmetry, only half of the two-dimensional model domain is discretized into a MINC grid, with a plan view of 1.0 m long and 0.1 (0.085 + 0.03/2) m wide. Along the fracture (sand layer), a one-dimensional, uniform linear grid of 200 elements was generated with $\Delta x = 0.005$ m, and a MINC mesh was made with 11 subdivisions (one fracture element with 10 matrix elements) for the 0.085 m thick matrix (silt layer), laterally connecting to the fracture elements. The rest of the properties used in the analysis are listed in Table 4. The input data of Table 4 are taken from those used by Sudicky et al. [37], except a non-zero matrix longitudinal dispersivity ($\alpha_{L,m} = 0.001$ m) and tortuosity values. The tortuosities are treated as calibration parameters.

We have performed a series of sensitivity analyses to the transport properties, as estimated by Sudicky et al. [37] and have found that the transport behavior of this experiment is controlled mainly by the matrix diffusion process during the entire breakthrough period. Therefore the combined matrix dispersion coefficients (2.3.2) and (2.3.3) is the most sensitive parameter to be calibrated for the problem. Since the dispersivities are fixed, we adjust only tortuosities for a better match, with the results given in Table 4. Fig. 6 shows the comparison between the laboratory and simulated breakthrough curves. The solid curve presents the numerical result using the parameters of Table 4, which matches the experimental results (triangles) reasonably well. However, this numerical solution cannot fit very well early breakthrough, at about 2 days, or the peak value, at about 9 days. A further examination of the parameters estimated in the test indicates that no measurement of sand porosity was made in the laboratory study, and it was assumed to be 0.33. The estimated pore velocity was therefore based on this assumed porosity value and may not be accurate. In their experiment, Sudicky et al. measured only the total volumetric flow rate, which was used in their analysis and canceled errors resulting from

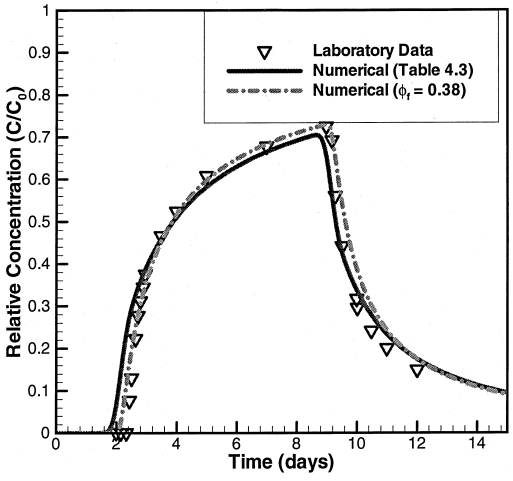

Fig. 6. Comparison of the simulated and laboratory measured breakthrough curves at the outlet of the sand layer.

Table 4
Parameters used in comparison with the laboratory testing results

Fracture aperture (sand layer thickness)	$b = 0.03$ m
Fracture (sand) porosity	$\phi_f = 0.33$
Matrix (silt) porosity	$\phi_m = 0.36$
Fracture (sand) permeability	$k_f = 2.11 \times 10^{-11}$ m^2
Matrix (silt) permeability	$k_m = 5.51 \times 10^{-15}$ m^2
Molecular diffusion coefficient	$D_m = 1.21 \times 10^{-9}$ m^2/s
Fracture longitudinal, transverse dispersivity	$\alpha_{L,f} = 0.001$ m, $\alpha_{T,f} = 0.0$
Matrix longitudinal, transverse dispersivity	$\alpha_{L,m} = 0.001$ m, $\alpha_{T,m} = 0.0$
Fracture–matrix dispersivity	$\alpha_{fm} = 0.0$
Fracture, matrix tortuosities	$\tau_f = 0.25$, $\tau_m = 0.5$
Matrix grain density	2650 kg/m^3
Fracture pore velocity	$v_{p,f} = 0.5$ m/d
Temperature	$T = 25$°C
Source pulse concentration	$C^{\text{radionuclide}} = 1.0$ for $t < 7$ d
Distribution coefficient in fractures and matrix	$K_{d,f} = K_{d,m} = 0.0$
Radioactive decay constant	$\lambda = 0.0$ s^{-1}

the assumed porosity value. In numerical studies, however, total volumetric flow rates are treated to be independent of porosity, and numerical results will be different for different sand porosity values, even though the flow rate is the same. If we keep Darcy's velocity or volumetric rate to be the same, we have

$$v_D = v_p\phi_f = 0.5 \times 0.33 = 0.165 \approx 0.43 \quad (= v_p) \times 0.38 \ (= \phi_f). \tag{4.2.1}$$

Using a pore velocity = 0.43 m/day and porosity = 0.38, the dashed curve of the numerical solution in Fig. 8 gives a better overall match with the experimental results.

4.3. Comparison of three-dimensional transport simulations with particle-tracking results

This example is to provide another verification case of the proposed scheme against particle-tracking modeling results, using a particle tracker, the DCPT code, recently developed for modeling transport in dual continua, fracture–matrix media by Pan et al. [26]. The test problem is based on the site-scale model developed for investigations of the unsaturated zone (UZ) at Yucca Mountain, Nevada [45,47]. It concerns transport of two radionuclides, one conservative (non-adsorbing) and one reactive (adsorbing), through fractured rock using a three-dimensional, unstructured grid and a dual-permeability conceptualization for handling fracture and matrix interactions.

The unsaturated zone of Yucca Mountain has been selected as a potential subsurface repository for storage of high-level radioactive wastes of the US. Since the mid-1980s, the US. Department of Energy has pursued a program of site characterization studies, designed to investigate the geological, hydrological, and geothermal conditions in the unsaturated and saturated zones of the mountain. The thickness of the unsaturated zone at Yucca Mountain varies between about 500 and 700 m, depending on local topography. The potential repository would be located in the highly fractured Topopah Spring welded unit (TSw), about 300 m above the water table and 300 m below the ground surface. The geologic formations are organized into hydrogeologic units roughly based on the degree of welding [21]. From the land surface downwards, we have the Tiva Canyon welded (TCw) hydrogeologic unit, the Paintbrush nonwelded unit (PTn), the TSw unit, the Calico Hills nonwelded (CHn), and the Crater Flat undifferentiated (CFu) units.

The three-dimensional model domain as well as a three-dimensional irregular numerical grid used for this comparison are shown for a plan view in Fig. 7. The model domain covers a total area of approximately 40 km^2, roughly from 2 km north of borehole G-2 in the north, to borehole G-3 in the south, and from the eastern boundary (Bow Ridge fault, not labeled) to about 1 km west of the Solitario Canyon fault. The model grid includes refined gridding along the ECRB and ESF, two underground tunnels, a number of boreholes (solid dots) used in site characterization studies and as references here, as well as several faults. Vertical profiles of geological layers and model grid are shown in Figs. 8 and 9, respectively, for west–east (Fig. 8) and south–north (Fig. 9) cross-sections. The potential repository is located in the middle of the model domain, an approximate area of 1000 m (west–east) by 5000 m (south–north), surrounded by the faults (Fig. 7). The repository is relatively flat and is represented by a number of 5-m-thick gridblocks, as shown in Figs. 8 and 9. The grid has 1434 mesh columns of fracture and matrix continua, respectively, and 37 computational grid layers in the vertical direction, resulting in 104 156 gridblocks and 421 134 connections in a dual-permeability grid.

The ground surface is taken as the top model boundary and the water table is regarded as the bottom boundary. Both top and bottom boundaries of the model are treated as Dirichlet-type boundaries, i.e.,

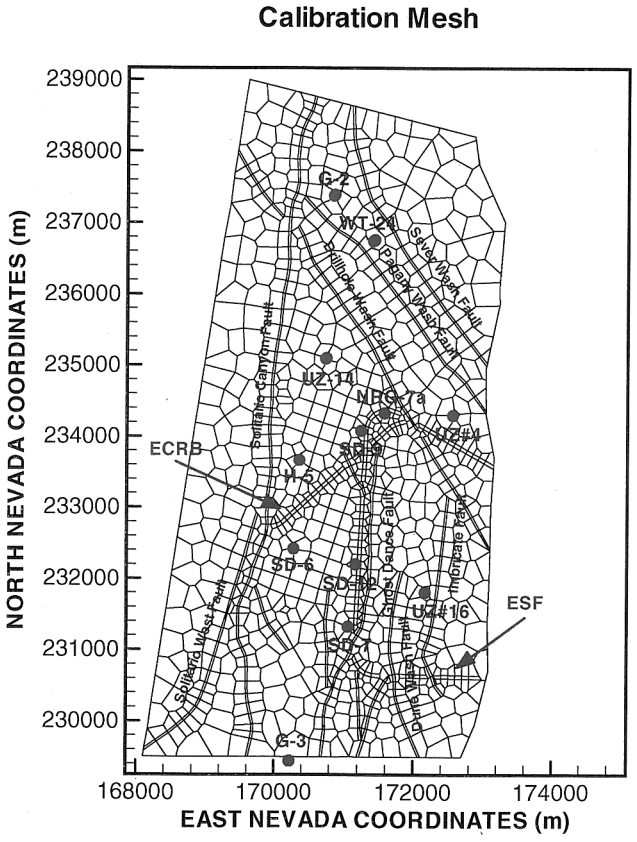

Fig. 7. Plan view of the three-dimensional UZ model grid, showing the model domain, faults incorporated, underground tunnels, and several borehole locations.

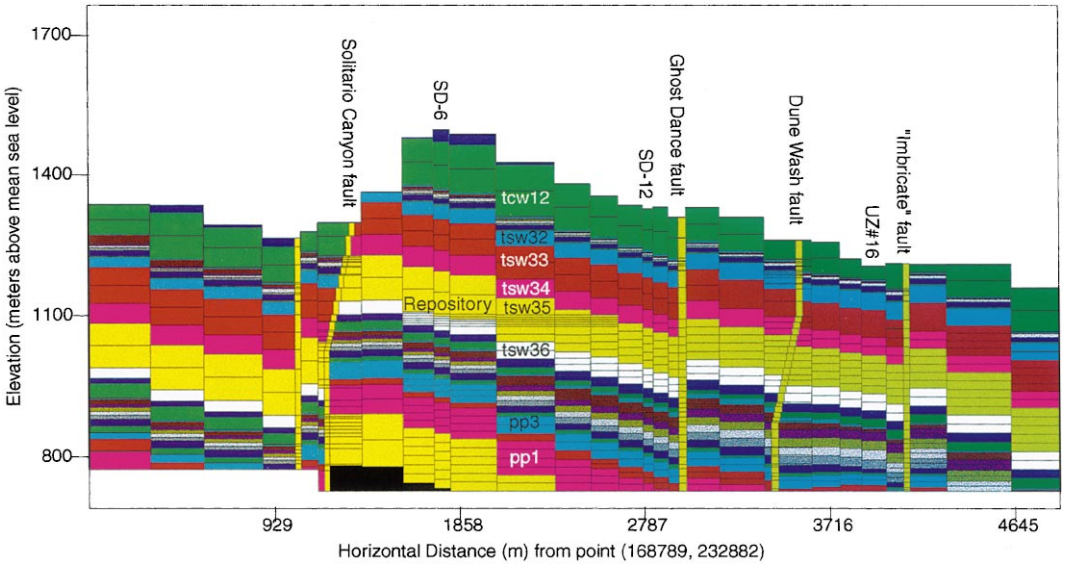

Fig. 8. West–east vertical cross-section through the three-dimensional UZ model crossing the southern model domain and boreholes SD-6, SD-12 and UZ#16, showing vertical profiles of geological layers, fault offsets, and the repository block.

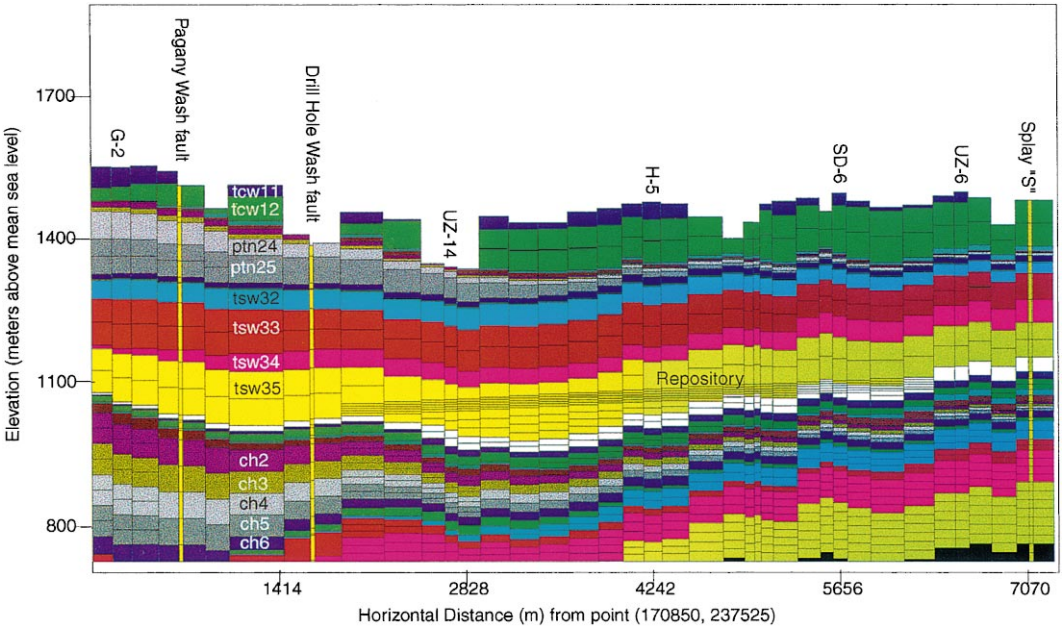

Fig. 9. North–south vertical cross-section through the three-dimensional UZ model crossing boreholes G-2, UZ-14, H-5, and SD-6, showing vertical profiles of geological layers, fault offsets, and the repository block.

constant (spatially distributed) pressures, liquid saturations and zero radionuclide concentrations are specified along these boundary surfaces. In addition, on the top boundary, a spatially varying, steady-state, present-day infiltration map, determined by the scientists in the US geological survey, is used in this study to describe the net water recharge, with an average infiltration rate of 4.56 mm/year over the model domain [47]. In addition, an isothermal condition is assumed in this study. The properties used for rock matrix and fractures for the dual-permeability model, including two-phase flow parameters of fractures and matrix, were estimated based on field tests and model calibration efforts, as summarized in [47].

We consider two types of radionuclides, technetium as a conservative tracer and neptunium as a reactive tracer. The initial conditions for the tracers correspond to the ambient condition, in which the flow field reaches

a steady-state under the net infiltration and stable water table conditions. The two radionuclides are treated as non-volatile and are transported only through the liquid phase. Radioactive decay and mechanical dispersion effects are ignored. A constant molecular diffusion coefficient of 3.2×10^{-11} (m^2/s) is used for matrix diffusion of the conservative component, and 1.6×10^{-10} (m^2/s) is used for the reactive component. In the case of a reactive or adsorbing tracer, several K_d values are used, as given in Table 5, and these values were selected to approximate those for neptunium, ^{237}Np, transport and for a conservative tracer, K_d is set to 0. All transport simulations were run to 1 000 000 years under a steady-state flow and initial, constant source concentration condition at the repository fracture blocks.

Two simulations were conducted, in which a finite amount of radionuclides is initially released into the fracture elements of the repository blocks. After the simulation starts, no more radionuclides will be introduced into the system, but the steady-state water recharge continues. Eventually, all the radionuclides will be flushed out from the system through the bottom, water table boundary by advective and diffusive processes.

Figs. 10 and 11 show comparisons between the simulated results using the proposed model (T2R3D) and the particle-tracking scheme (DCPT) for non-adsorbing and adsorbing tracers, respectively. In the figures, the fractional mass breakthrough at the water table is defined as the cumulative mass of radionuclides crossing the entire model bottom boundary over the time, normalized by the total initial mass. In both cases, the simulation results using the two types of modeling approaches are in good agreement, as shown in Figs. 10 and 11, for the entire simulation period of 10^6 years of transport through fractured formation. In addition, the good match, shown in Figs. 10 and 11, indicate little numerical dispersion in the modeling results of T2R3D for the problem, because there is no numerical dispersion in the particle-tracking results.

Table 5
K_d values used for a reactive tracer transport in different hydrogeologic units

Hydrogeologic unit	K_d (cm^3/g)
Zeolitic matrix in CHn	4.0
Vitric matrix in CHn	1.0
Matrix in TSw	1.0
Fault matrix in CHn	1.0
Fractures and the matrix in the rest of units	0.0

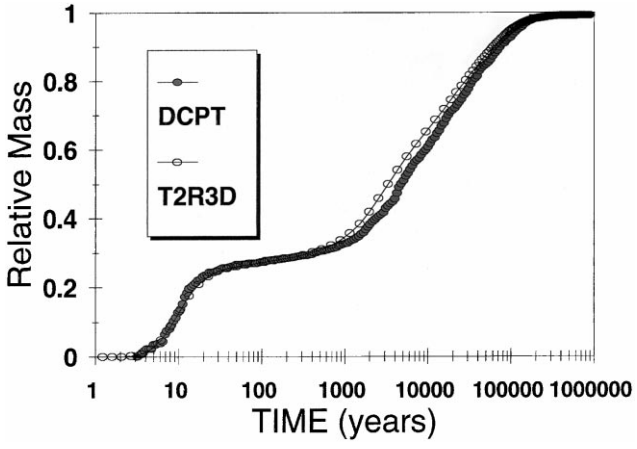

Fig. 10. Comparison of relative mass breakthrough curves of a conservative tracer arriving at the water table, simulated using the present model and a particle-tracking scheme.

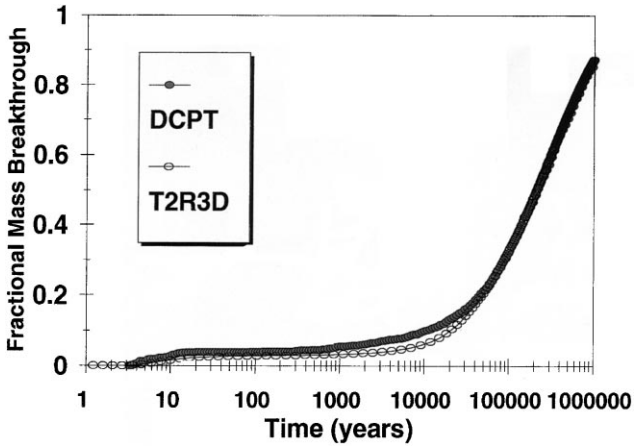

Fig. 11. Comparison of relative mass breakthrough curves of a reactive tracer arriving at the water table, simulated using the present model and a particle-tracking scheme.

The mass breakthrough curves of Figs. 10 and 11 reveal an interesting phenomenon of tracer transport through fractured rock, i.e., there is a plateau between the earlier and later times of the rapid increases. This is a typical behavior of transport through a dual-continua medium, the earlier, rapid breakthrough is due to transport through fast fracture flow and the later, rapid increase in mass transport corresponds to massive breakthrough occurring through the matrix. Along the plateau portion of the breakthrough curve, little mass arrives at the water table, and this is because matrix breakthrough is lagging behind fracture breakthrough.

5. Application examples

Because of the generalized capability of the proposed model in handling tracer and radionuclide transport through multiphase, non-isothermal, and fractured medium systems, the implemented modules of the T2R3D code [49] have found a wide range of applications in field characterization studies at the Yucca Mountain site [3,47]. The methodology discussed above has been used

as a main modeling approach in three-dimensional, large-scale unsaturated zone model calibrations [53] and in modeling geochemical transport [36].

We present two application examples in this section to demonstrate the applicability of the new transport-modeling approach to field problems, including:

- three-dimensional liquid radionuclide transport in unsaturated fractured rock; and
- two-dimensional gas tracer transport in unsaturated fractured rock including thermal effects.

5.1. Three-dimensional radionuclide transport in unsaturated fractured rocks

This example uses the same setup of the problem in Section 4.3, including the model domain, numerical grid (Fig. 7), modeling approach, parameters, and description of initial and boundary conditions. The same two radionuclides, conservative technetium and reactive neptunium, are simulated. In conducting this modeling exercise, we found that dispersion effects on matrix–matrix and fracture–matrix transport are negligible for the fracture–matrix system under study, when compared with advection or molecular diffusion terms. Therefore, only dispersion effects through fracture–fracture transport are included in this study, using longitudinal and transverse dispersivities of 10 and 1 m, respectively.

The objective of this example is to apply the proposed model to a sensitivity analysis of effects of different hydrogeological conceptual models and infiltration on adsorbing and non-adsorbing transport processes of radionuclides from the repository to the water table at Yucca Mountain. Modeling scenarios incorporate three hydrogeological conceptual models on perched water occurrence and three surface water recharge rates of mean, lower-bound and upper-bound infiltration maps, with averaged values of 4.56, 1.20 and 11.28 (mm/year), respectively, over the model domain. In all simulations, a flow simulation was conducted first and then followed by a transport run under the same flow condition. The flow simulation was used to provide a steady-state flow field for the following simulation scenario, in which different conceptual models combining with different infiltration rates are considered.

A total of 14 transport simulations were conducted in this study, as listed in Table 6. The three hydrogeological conceptual models, regarding perched water occurrence, are incorporated in flow simulations. They are:

1. non-water-perching model (no perched water conditions will be generated in the unsaturated zone);
2. flow-through perched water model (perched water zones will be generated in the unit below the repository with significant amount of water vertically flowing through perched zones);
3. by-passing perched water model (perched water zones will be generated in the unit below the repository with significant lateral flow on perched zones) [47].

In Table 6 the letter of simulation designation, ending with a represents transport simulation for conservative/non-adsorbing tracer/radionuclide and that ending with b is for reactive/adsorbing tracer/radionuclide transport.

Simulation results, in terms of fractional mass breakthrough, is presented in Fig. 12 for the 14 simulations. In the figure, solid-line curves represent simulation results of conservative/non-adsorbing tracer transport and dotted-line plots are for reactive, adsorbing tracer transport. Fig. 12 shows a wide range of radionuclide transport times with different infiltration rates, types of radionuclides, and perched water conceptual models from the 14 simulations. The predominant factors for transport or breakthrough times, as indicated by the figure, are: (1) surface-infiltration rates and (2) adsorption effects, whether the tracer is conservative or reactive. To a certain extent, perched water conceptual models also affect transport times significantly, but their overall impacts are secondary compared with effects by infiltration and adsorption. The simulation results, as shown in Fig. 12, can be used to

Table 6
Fourteen radionuclide transport simulation scenarios (hydrological conceptual models and infiltration rates)

Designation	Hydrogeological model	Infiltration rate
TR#1a	Non-water-perching	Mean
TR#1b		
TR#2a	Flow-through perched water	Lower-bound
TR#2b		
TR#3a	By-passing perched water	Lower-bound
TR#3b		
TR#4a	Flow-through perched water	Mean
TR#4b		
TR#5a	By-passing perched water	Mean
TR#5a		
TR#6a	Flow-through perched water	Upper-bound
TR#6b		
TR#7a	By-passing perched water	Upper-bound
TR#7b		

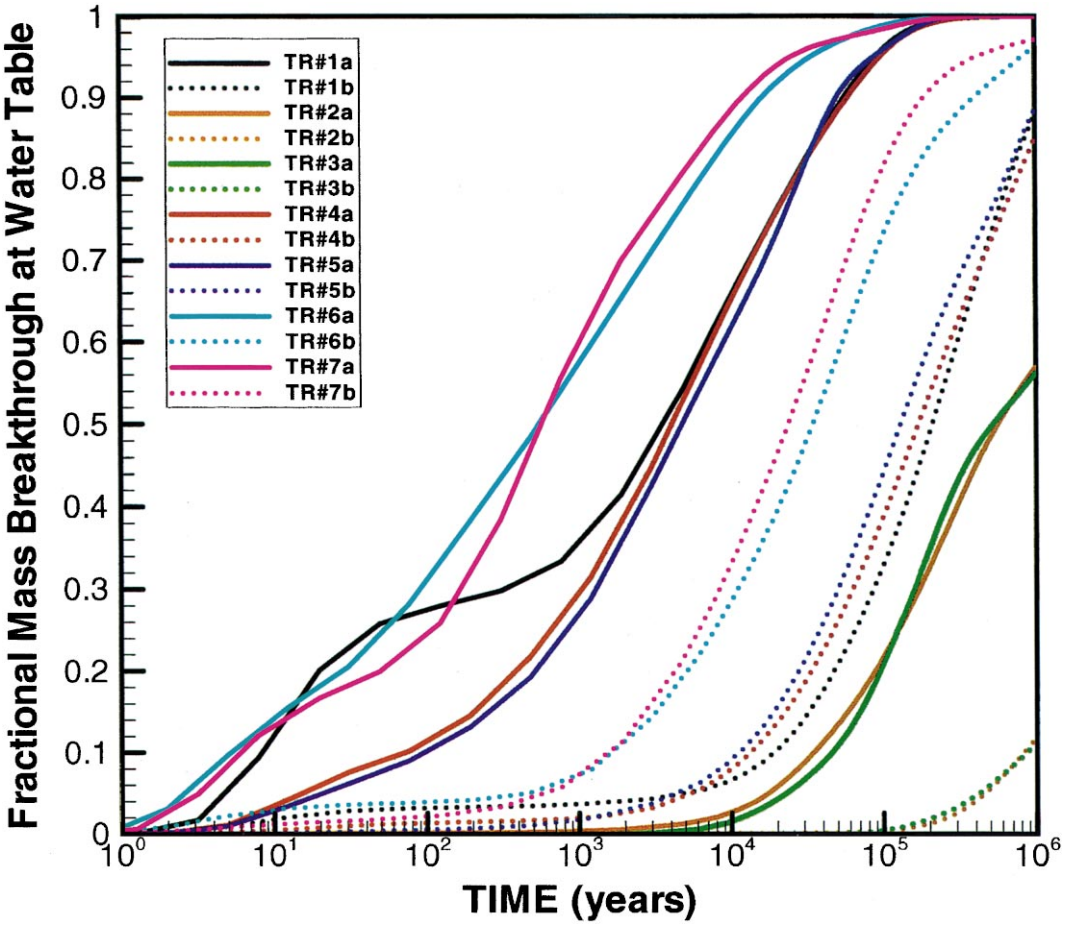

Fig. 12. Simulated breakthrough curves of cumulative radionuclide mass arriving at the water table, since releasing from the repository, using the three infiltration scenarios and three hydrogeological conceptual models.

obtain insights of radionuclide transport through the unsaturated zone system of Yucca Mountain, taking into account future climatic conditions, various radionuclides and different hydrogeological conceptual models.

5.2. Two-dimensional gas tracer transport with thermal effects

The second example is a sensitivity study of gaseous radionuclide transport in the unsaturated zone at Yucca Mountain with the repository thermal load effects. Under natural hydrological and geothermal conditions, both liquid and gas (air and vapor) flow in the unsaturated zone of the mountain are affected by ambient temperature changes, geothermal gradients, as well as atmospheric and water table conditions. Thermal and hydrological regimes are closely related through coupling of heat, gas and liquid flow, and atmospheric conditions at the mountain [44,45]. In addition to the ambient thermal conditions, heat will be generated as a result of emplacing high-level nuclear waste in the repository drifts of the unsaturated zone. Thermal loading from the waste repository will significantly affect the post-waste emplacement performance of the repository, and will create complex multiphase fluid flow and heat transfer processes [50]. Certain gaseous radionuclide, such as C-14, may be released as gaseous components from the repository under thermal–hydrological effects, and may be escaped into the atmosphere at the land surface. Gas tracer transport is coupled with other processes, such as conductive and convective heat transfer, phase change (vaporization and condensation), capillary- and gravity-driven two-phase flow under variably-saturated conditions, and diffusion and dispersion of water and air components.

A dual-permeability approach is also used for fracture–matrix interactions in this study. A two-dimensional west–east, vertical cross-section model is selected along the middle of the repository near Borehole SD-9, as shown in Fig. 12 for the entire model domain. The irregular vertical grid, which includes four inclined faults, is designed for this two-dimensional cross-section, as displayed in Fig. 13. The grid is locally refined at the repository horizon with three 5-m-thick layers and the actual repository length along the section. The grid

has a horizontal spacing of 28 m, and an average vertical spacing of 10 m. A continuously decaying heat source is applied in the gridblocks throughout the repository. The two-dimensional model has approximately 18 000 fracture and matrix elements, and 44 000 connections.

The boundary conditions are similar to those used by the three-dimensional model of Section 5.1. The ground surface (or the tuff-alluvium contact, in areas of significant alluvial cover) is taken as the top model boundary. The water table is taken as the bottom boundary with fixed, spatially varying temperatures specified. The surface infiltration map [7] is implemented as source terms to the fracture gridblocks in the upper boundary and the resulting infiltration rates varying along each gridblock, with an average of 3.67 mm/year along the cross-section.

The initial conditions for the gas tracer simulation were generated using steady-state simulation results under the ambient moisture, infiltration and thermal conditions. The simulated initial matrix liquid saturation is about 0.90–0.95 at the repository level, which agrees with the observed data at a nearby borehole, SD-9. The average initial temperature is about 25°C at the repository horizon.

A thermal loading scenario of 85 MTU/acre (Metric Tons of Uranium/acre) and a thermal decay curve of the repository heat, considered as the base–case [14] for the repository performance analysis is used for thermal calculations. Thermal loading is expressed in terms of areal mass loading (AML) (MTU/acre), or areal power density (APD) (kW/acre) to account for radioactive heat of decay. AML or APD values per waste type in a given repository design will determine the total thermal energy introduced into the system or heat released from the source. The thermal load for use in these studies is an average for mixed wastes (commercial and non-commercial spent fuels), corresponding to APD = 99.4 kW/acre.

Fluid and rock properties for this problem are taken from those for the recent modeling studies at Yucca Mountain [3]. The properties of tracer transport are listed in Table 7. Because of the lack of measured field data, we ignore the effects of hydrodynamic dispersion in this case. The gas tracer is treated as a conservative species without decay. The liquid/gas phase partitioning coefficient was estimated based on CO_2 property. Even though the equilibrium constant may be a function of both pH and temperature, an averaged value of 281 is used in this study, which corresponds to pH = 7 and $T = 50$°C for CO_2.

In addition to surface water infiltration and heat release at the repository, a constant gas tracer generation rate of 1 g/day is introduced in each repository block. Here, both heat and gas tracer sources are injected only into repository matrix blocks, not fracture blocks. The objective of this sensitivity study is to investigate the migration, distribution, and releasing of the gas tracer under repository thermal effects. Simulation times are up to 100 000 years.

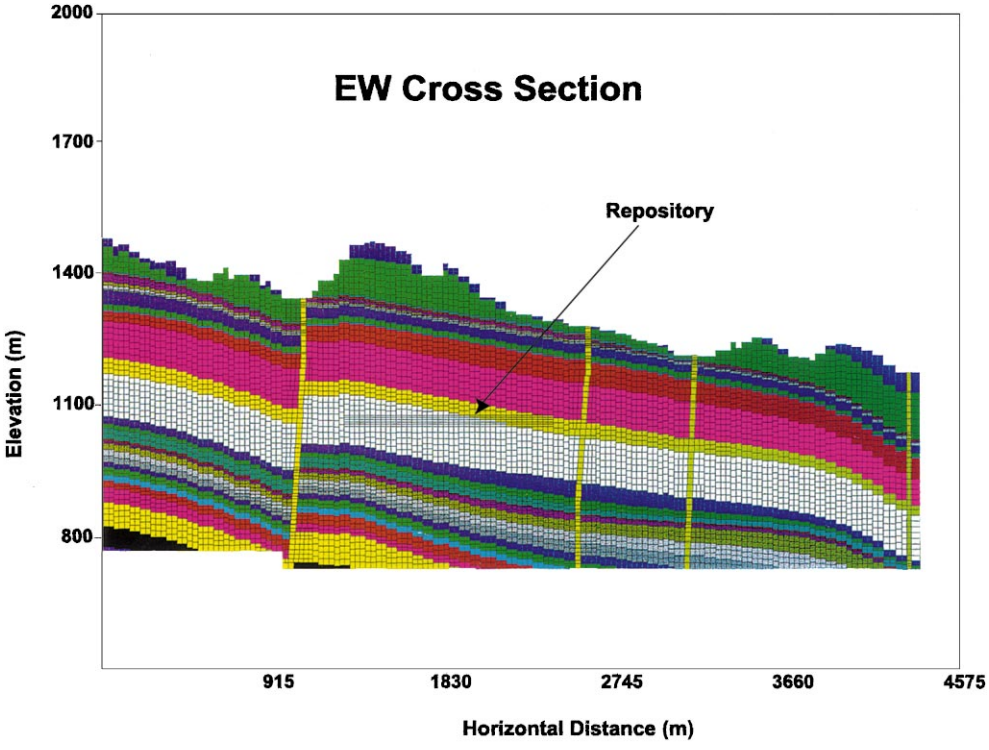

Fig. 13. Two-dimensional west–east cross-section grid, showing the vertical layering, faults and location of the repository.

Table 7
Parameters for gas tracer transport under thermal effects

Molecular diffusion coefficient in gas	$D_m = 2.13 \times 10^{-5}$ m^2/s
Molecular diffusion coefficient in liquid	$D_m = 1.0 \times 10^{-10}$ m^2/s
Fracture longitudinal, transverse dispersivity	$\alpha_{L,f} = 0.0$, $\alpha_{T,f} = 0.0$
Matrix longitudinal, transverse dispersivity	$\alpha_{L,m} = 0.0$, $\alpha_{T,m} = 0.0$
Fracture–matrix dispersivity	$\alpha_{fm} = 0.0$
Fracture, matrix tortuosities	$\tau_f = 0.7$, $\tau_m = 0.7$
Distribution coefficients in matrix and fractures of all units	$K_{d,f} = K_{d,m} = 0.0$
Equilibrium phase partitioning coefficient	$K_P = 281$
Radioactive decay constant	$\lambda = 0.0$ s^{-1}

Fig. 14 shows the changes in temperature and moisture conditions at the center of the repository versus time, after thermal loading is imposed in the repository. The figure indicates a rapid increase in temperature at the repository after thermal load starts, reaching the boiling point (97°C) at ambient pressure about 10 years after waste emplacement. At this time, fractures at the repository become completely dry and matrix liquid saturation decreases significantly. Temperature continues to rise at the repository afterwards and reaches a peak of 140°C after 100 years, then gradually decreases as heat input is reduced. However, boiling conditions are still prevalent and last for several thousand years. As a result, dryout continues in both fractures and matrix blocks at and near the repository during this period.

Figs. 15 and 16 present simulated temperature conditions after 100 and 1000 years, respectively, showing that an extensive boiling zone develops around the repository in 100 years, which becomes larger after 1000 years. The normalized (relative to the highest concentration at the time in the system) concentration contours of the gas tracer are shown in Figs. 17 and 18 for these two times. It is interesting to note that (1) the highest concentrations of the gas tracer in the gas phase are not at or near the source (repository blocks) and (2) the high concentration zones change dynamically with time. This results from the effects of the boiling zones surrounding the repository, within which a large amount of liquid water turns into steam, increasing gas flow rates by several orders of magnitude with vapor mass fraction up to 95% or higher in the gas phase. At some distance from the repository, vapor is removed by condensation, which causes gaseous radionuclide concentration to increase. At the same time, the high gas flux at and near the boiling zones rapidly moves away from the repository and effectively "dilutes" concentrations of the gas tracer in these regions, since a constant radionuclide mass generation rate is specified at the repository.

Fig. 19 shows the simulated surface-mass release rate of the gas tracer, normalized to the total generation rate

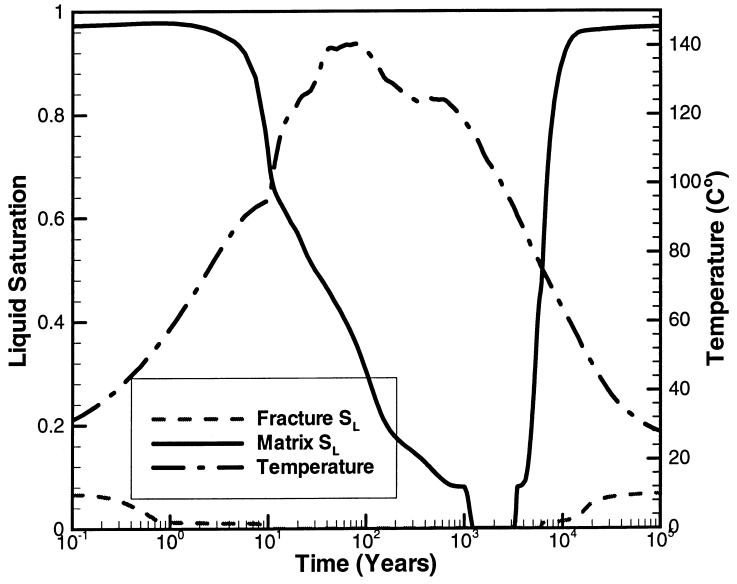

Fig. 14. Changes in fracture and matrix liquid saturations, and temperatures at the repository under thermal load, simulated using the two-dimensional vertical cross-section model.

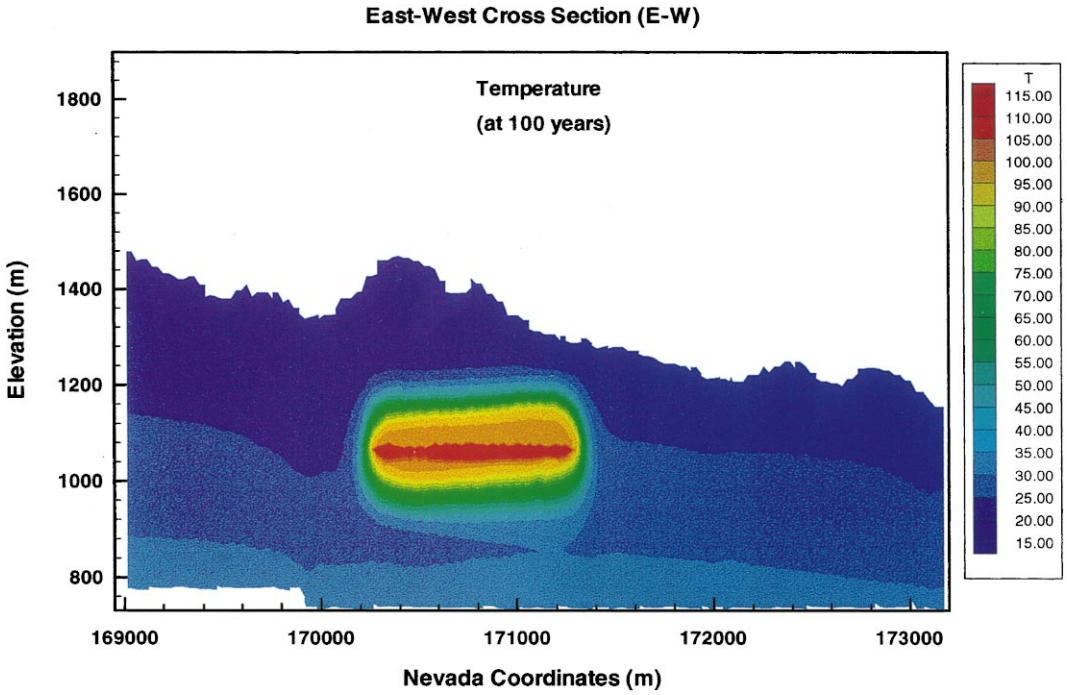

Fig. 15. Temperature contours at 100 years of thermo load, simulated using the two-dimensional vertical cross-section model.

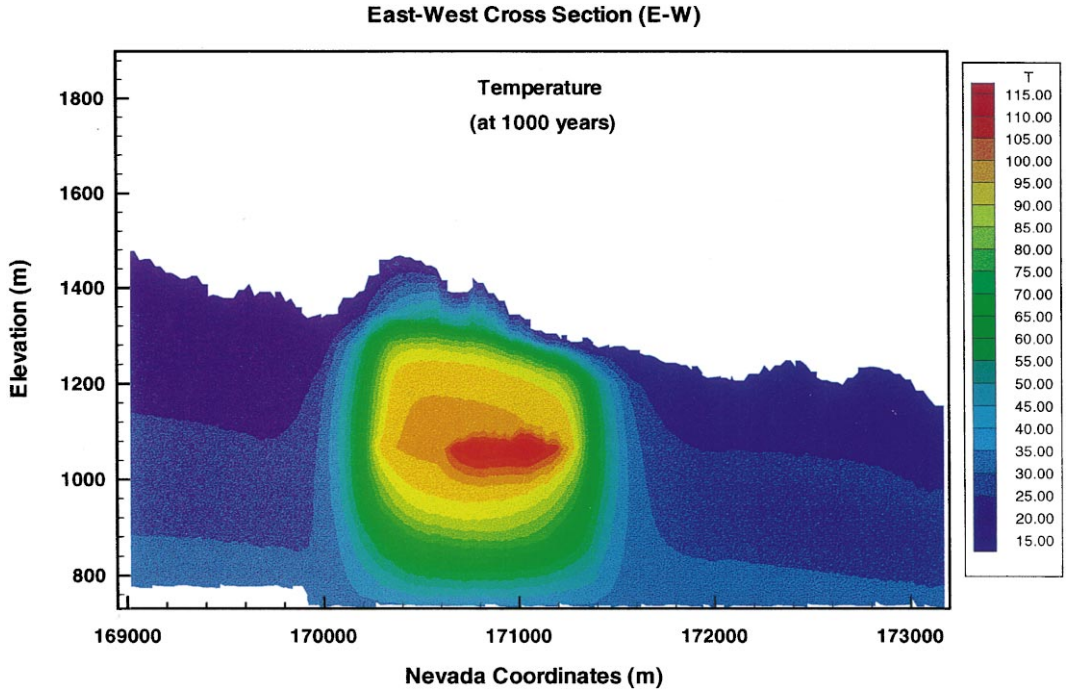

Fig. 16. Temperature contours at 1000 years of thermo load, simulated using the two-dimensional vertical cross-section model.

at the repository. The figure indicates that the breakthrough of a gas tracer associated with thermal loading at the repository occurs after about 100 years of waste emplacement. The surface-release rate of the gas tracer reaches its peak value after 1000 years and then stabilizes at 90% of the total generation rate.

6. Summary and conclusions

A new numerical approach has been developed for modeling tracer or radionuclide transport through heterogeneous fractured rocks in a non-isothermal multiphase system. The model formulation incorporates a full

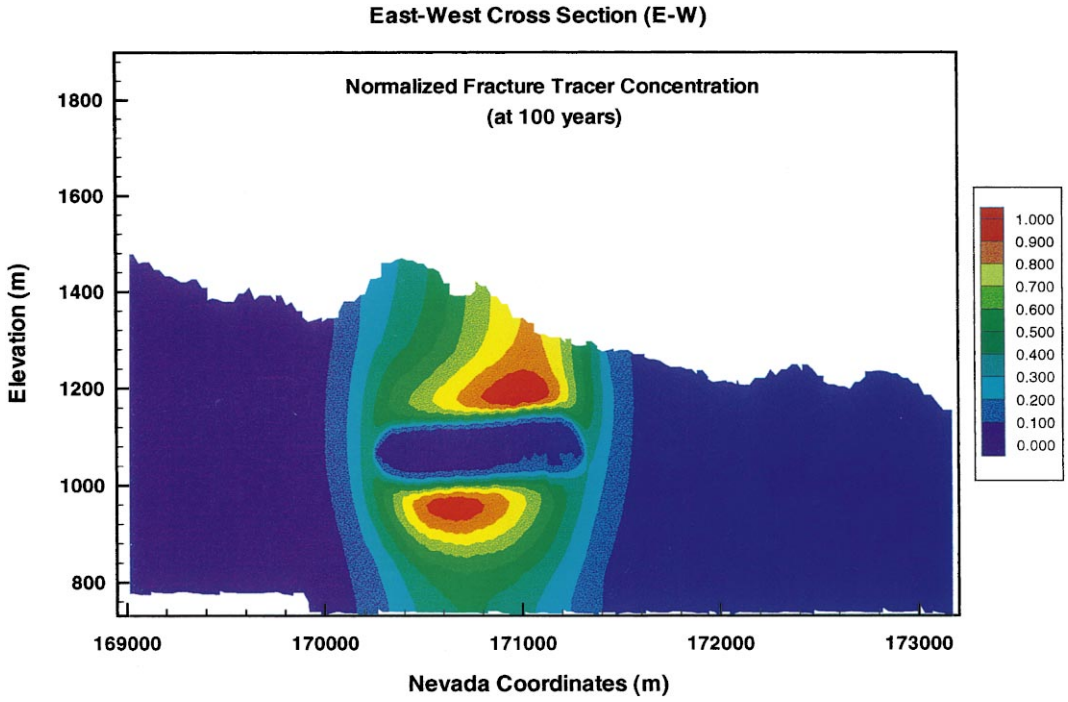

Fig. 17. Gas tracer concentration contours at 100 years of thermo load, simulated using the two-dimensional vertical cross-section model.

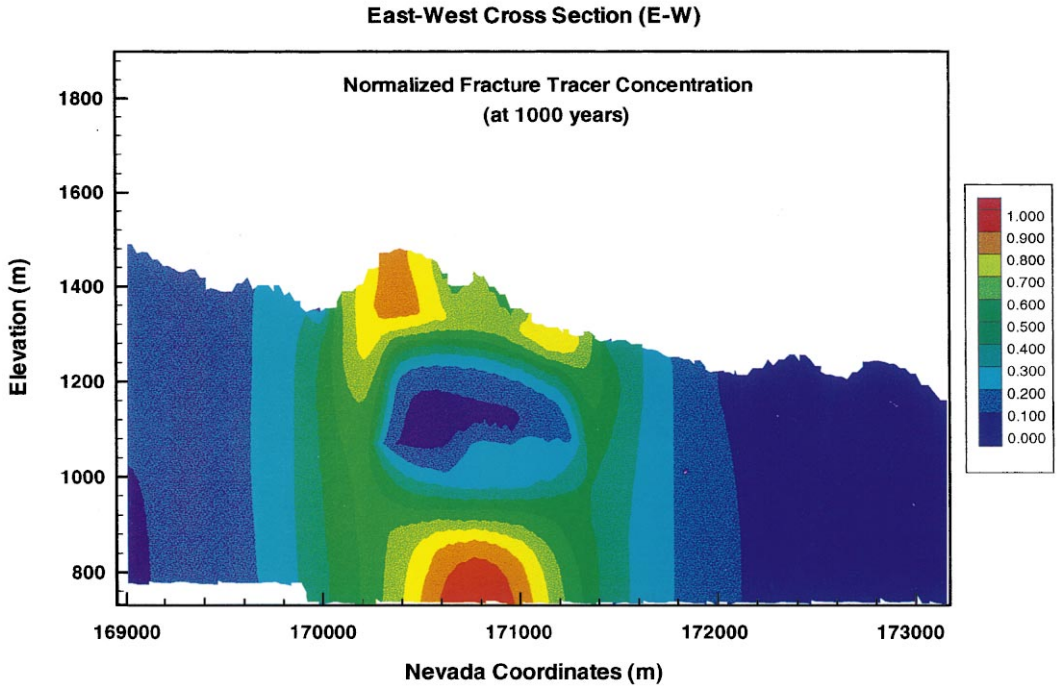

Fig. 18. Gas tracer concentration contours at 1000 years of thermo load, simulated using the two-dimensional vertical cross-section model.

hydrodynamic dispersion tensor using a three-dimensional regular or irregular grid. Two different weighting schemes are tested for accurate spatial interpolation of three-dimensional velocity fields and concentration gradients to evaluate the mass flux by dispersion and diffusion of a tracer or radionuclide. The fracture–matrix interactions are handled using a dual-continua approach, such as a double- or multiple-porosity or dual-permeability. This new method has been implemented into a multidimensional numerical code of

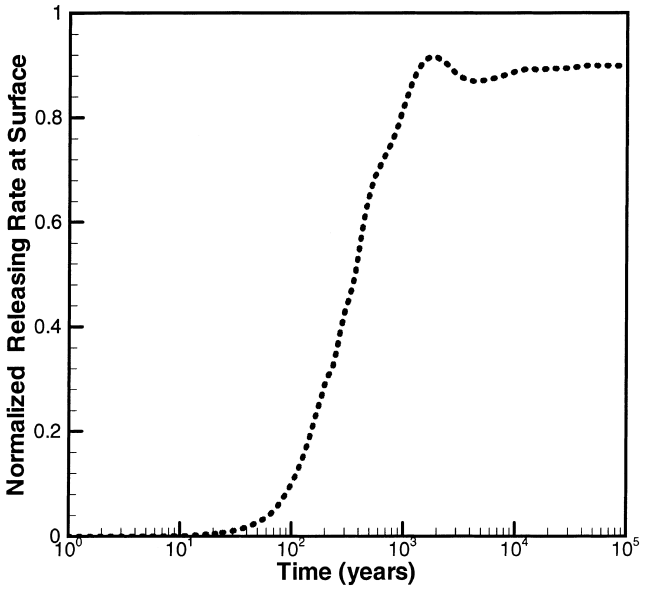

Fig. 19. Surface release rate of the gas tracer showing the repository thermal effects, simulated using the two-dimensional vertical cross-section model.

integral finite-difference to simulate processes of tracer or radionuclide transport in non-isothermal, three-dimensional, multiphase, fractured and/or porous subsurface systems.

We have verified this new transport-modeling approach by comparing its results to those from an analytical solution for a parallel-fracture transport problem, a published laboratory study, and a particle-tracking scheme for three-dimensional transport using an unstructured grid. In addition, two examples of field applications are presented to demonstrate the use of the proposed methodology for modeling three-dimensional transport of liquid radionuclides and gas tracer transport with thermal effects in unsaturated fractured rocks.

The model formulation and the implemented code have found a wide range of applications in field characterization studies of the unsaturated-zone transport of environmental isotopic tracers and radionuclides at the Yucca Mountain site. The special capability of modeling tracer transport processes through heterogeneous, fractured rocks under multiphase and non-isothermal conditions with full consideration of hydrodynamic dispersion will make the model a very useful tool in studies of tracer transport in other areas, such as reservoir engineering.

Acknowledgements

The authors would like to thank many of their colleagues at Lawrence Berkeley National Laboratory for their suggestions and encouragement for this work. In particular, the authors are grateful to S. Finsterle and T. Xu for their critical review of this paper. Thanks are due to Lehua Pan, C. Oldenburg, N. Spycher and W. Zhang for their help in this work. Thanks are also due to E.A. Sudicky for providing a computer program of the analytical solution used in a benchmarking problem. This work was supported by the Assistant Secretary for Energy Efficiency and Renewable Energy, Office of Geothermal and Wind Technologies of the US Department of Energy and by the Director, Office of Civilian Radioactive Waste Management, US Department of Energy, through Memorandum Purchase Order EA9013MC5X between TRW Environmental Safety Systems Inc. and the Ernest Orlando Lawrence National Laboratory. The support is provided to Berkeley Lab through the US Department of Energy Contract No. DE-AC03-76SF00098.

References

[1] Aziz K, Settari A. Petroleum reservoir simulation. London: Applied Science Publishers, 1979.
[2] Barenblatt GI, Zheltov IP, Kochina IN. Basic concepts in the theory of seepage of homogeneous liquids in fissured rocks, PMM. Sov Appl Math Mech 1960;24(5):852–64.
[3] Bodvarsson GS, Bandurraga TM, Wu YS, editors. The site-scale unsaturated zone model of Yucca Mountain, Nevada, for the viability assessment. Yucca Mountain Site Characterization Project Report, LBNL-40376, UC-814, Lawrence Berkeley National Laboratory, Berkeley, CA, 1997.
[4] Fabryka-Martin JT, Wolfsberg AV, Dixon PR, Levy S, Musgrave J, Turin HJ. Chlorine-36 in the exploratory studies facility. Report LA-CST-TIP-96-002, Milestone 3783AD, Los Alamos National Laboratory, Los Alamos, NM, 1996.
[5] Falta WR, Pruess K, Javandel I, Witherspoon PA. Numerical modeling of steam injection for the removal of nonaqueous phase liquids from the subsurface, 1. Numerical formulation. Water Resour Res 1992;28(2):433–49.
[6] Falta WR, Pruess K, Javandel I, Witherspoon PA. Numerical modeling of steam injection for the removal of nonaqueous phase liquids from the subsurface, 2. Code validation and application. Water Resour Res 1992;28(2):451–65.
[7] Flint AL, Hevesi JA, Flint EL. Conceptual and numerical model of infiltration for the Yucca Mountain area, Nevada. US Geological Survey. Water-Resources Investigation Report-96, Denver, CO, 1996.
[8] Fogden A, Landman KA, White LR. Contaminant transport in fractured porous media: steady-state solutions by a boundary integral method. Water Resour Res 1988;8(8):1384–96.
[9] Forsyth PA, Unger AJA, Sudicky EA. Nonlinear iteration methods for nonequilibrium multiphase subsurface flow. Adv Water Resour 1998;21:433–99.
[10] Forsyth PA, Kropinski MC. Monotonicity considerations for saturated-unsaturated subsurface flow. SIAM J Sci Comput 1997;18(5):1328–54.
[11] Forsyth PA, Wu YS, Pruess K. Robust numerical methods for saturated-unsaturated flow with dry initial conditions in heterogeneous media. Adv Water Resour 1995;18:25–38.
[12] Forsyth PA. Three-dimensional modeling of steam flush for DNAPL site remediation. Int J Numer Meth Fluids 1994;19:1055–81.

[13] Forsyth PA. MATB user's guide: iterative sparse matrix solvers for block matrices. University of Waterloo, Waterloo, Ont., Canada, 1992.
[14] Francis ND. Repository thermal loading for TSPA-VA calculations. In: Proceedings of the Eight International Conference, High-Level Radioactive Waste Management, ANS, 11–14 May, Las Vegas, NV, 1998. p. 755–57.
[15] Haggerty R, Gorelick SM. Multiple-rate mass transfer for modeling diffusion and surface reactions in a media with pore-scale heterogeneity. Water Resour Res 1995;31(10):2383–400.
[16] Huyakorn PS, Lester BH, Mercer JW. An efficient finite element technique for modeling transport of fractured porous media, 1. Single species transport. Water Resour Res 1983; 19(3):841–54.
[17] Huyakorn PS, Pinder GF. Computational methods in subsurface flow. New York: Academic Press, 1983.
[18] Istok J. Groundwater modeling by the finite element method. American Geophysical Union Water Resources Monograph, no. 13, 1989.
[19] Kazemi H. Pressure transient analysis of naturally fractured reservoirs with uniform fracture distribution. SPEJ (Trans AIME) 246;1969:451–62.
[20] Lichtner PC, Seth M. Multiphase-multicomponent nonisothermal reactive transport in partially saturated porous media. In: Proceedings of the International Conference on Deep Geological Disposal of Radioactive Waste, Canadian Nuclear Society, 1996. p. 3-133–42.
[21] Montazer P, Wilson WE. Conceptual hydrologic model of flow in the unsaturated zone, Yucca Mountain, Nevada. US Geological Survey, Water Resources Investigations Report 84-4345, 1984.
[22] Narasimhan TN, Witherspoon PA. An integrated finite difference method for analyzing fluid flow in porous media. Water Resour Res 1976;12(1):57–64.
[23] Oldenburg CM, Pruess K. Higher-order differencing for geothermal reservoir simulation. In: Proceedings of the 22nd Workshop on Geothermal Reservoir Engineering, Stanford University, Stanford, CA, January 1997. p. 27–9.
[24] Oldenburg CM, Pruess K. EOS7R: radionulcide transport for TOUGH2. Report LBL-34868, UC-800, Lawrence Berkeley National Laboratory, Berkeley, CA, 1995.
[25] Oldenburg CM, Pruess K. A two-dimensional dispersion module for the TOUGH2 simulator. Report LBL-32505, Lawrence Berkeley National Laboratory, Berkeley, CA, 1993.
[26] Pan L, Liu HH, Cushey M, Bodvarsson GS. DCPT – a new particle tracker for modeling transport in dual continuum media. Report LBNL-42958, Lawrence Berkeley National Laboratory, Berkeley, CA, 1999.
[27] Panday S, Forsyth PA, Falta RW, Wu YS, Huyakorn PS. Considerations for robust compositional simulations of subsurface nonaqueous phase liquid contamination and remediation. Water Resour Res 1995;31(5):1273–89.
[28] Peaceman DW. Fundamentals of numerical reservoir simulation. In: Developments in petroleum sciences, vol. 6. Amsterdam: Elsevier, 1977.
[29] Pruess K. TOUGH2 – a general-purpose numerical simulator for multiphase fluid and heat flow. Report LBL-29400, Lawrence Berkeley National Laboratory, Berkeley, CA, 1991.
[30] Pruess K. TOUGH User's Guide. Nuclear Regulatory Commission, Report NUREG/CR-4645, Report LBL-20700, Lawrence Berkeley National Laboratory, Berkeley, CA, 1987.
[31] Pruess K, Narasimhan TN. A practical method for modeling fluid and heat flow in fractured porous media. Soc Pet Eng J 1985;25:14–26.
[32] Pruess K. GMINC – a mesh generator for flow simulations in fractured reservoirs. Report LBL-15227, Lawrence Berkeley National Laboratory, Berkeley, CA, 1983.
[33] Pruess K, Narasimhan TN. On fluid reserves and the production of superheated steam from fractured vapor-dominated geothermal reservoirs. J Geophys Res B 1982;87(11):9329–39.
[34] Rasmuson A, Narasimhan TN, Neretnieks I. Chemical transport in a fissured rock: verification of a numerical model. Water Resour Res 1982;18(3):1479–92.
[35] Scheidegger AE. General theory of dispersion in porous media. J Geophys Res 1961;66:3273–8.
[36] Sonnenthal EL, Bodvarsson GS. Modeling the chloride geochemistry in the unsaturated zone. In: Bodvarsson GS, Bandurraga TM, Wu YS, editors. The site-scale unsaturated zone model of Yucca Mountain, Nevada, for the viability assessment. Yucca Mountain Project, Level 4 Milestone SP24UFM4; Report LBNL-40376, UC-814, Lawrence Berkeley National Laboratory, Berkeley, CA, 1997 (Chapter 15).
[37] Sudicky EA, Gillgam RW, Frind EO. Experimental investigation of solute transport in stratified porous media, 1. The nonreactive case. Water Resour Res 1985;21(7):1035–41.
[38] Sudicky EA, Frind EO. Contaminant transport in fractured porous media: analytical solutions for a system of parallel fractures. Water Resour Res 1982;18(6):1634–42.
[39] Tsang YW, Pruess K. Further modeling studies of gas movement and moisture migration at Yucca Mountain, Nevada. LBL-29127, Lawrence Berkeley National Laboratory, Earth Sciences Division, Berkeley, CA, 1990.
[40] Unger AJA, Forsyth PA, Sudicky EA. Variable spatial and temporal weighting schemes for use in multi-phase compositional problems. Adv Water Res 1996;19(1):1–27.
[41] van Genuchten MTh, Dalton FN. Models for simulating salt movement in aggregated field soils. Geoderma 1986;38:165–83.
[42] Viswanathan HS, Robinson BA, Valocchi AJ, Triay IR. A reactive transport model of neptuniun migration from the potential repository at Yucca Mountain. J Hydrol 1998;209:251–80.
[43] Warren JE, Root PJ. The behavior of naturally fractured reservoirs. Soc Pet Eng J (Trans AIME) 228;1963:245–255.
[44] Weeks EP. Effect of topography on gas flow in unsaturated fractured rock: concepts and observations. In: Evans DD, Nicholson TJ, editors. Flow and transport through unsaturated fractured rock. Geophysical Monograph 42. Washington, DC: American Geophysical Union, 1987. p. 165–70.
[45] Wu YS, Haukwa C, Bodvarsson GS. A site-scale model for fluid and heat flow in the unsaturated zone of Yucca Mountain, Nevada. J Contam Hydrol 1999;38(1–3):185–215.
[46] Wu YS. A virtual node method for treatment of wells in modeling multiphase flow in reservoirs. In: Proceedings of the 24th Workshop, Geothermal Reservoir Engineering, Stanford University, CA, 1999.
[47] Wu YS, Liu J, Xu T, Haukwa C, Zhang W. UZ flow models and submodels. Yucca Mountain Project, AMR Report, MDL-NBS-HS-000006, Lawrence Berkeley National Laboratory, Berkeley, CA, 1999.
[48] Wu YS, Pruess K. A 3D hydrodynamic dispersion model for modeling tracer transport in geothermal reservoirs. In: Proceedings of the 23rd Workshop, Geothermal Reservoir Engineering, Stanford University, CA, 1998. p. 139–146.
[49] Wu YS, Ahlers CF, Fraser P, Simmons A, Pruess K. Software qualification of selected TOUGH2 modules. Report LBL-39490, UC-800, Lawrence Berkeley National Laboratory, Berkeley, CA, 1996.
[50] Wu YS, Chen G, Bodvarsson GS. Preliminary analysis of effects of thermal loading on gas and heat flow within the framework of the LBNL/USGS site-scale model. Research Report LBL-37229, UC-814, Lawrence Berkeley National Laboratory, Berkeley, CA, 1995.
[51] Wu YS, Pruess K. A multiple-porosity method for simulation of naturally fractured petroleum reservoirs. SPE Reservoir Eng 1988;3:327–36.

[52] Xu T, Gerard FG, Pruess K. Modeling non-isothermal multiphase multi-species reactive chemical transport in geologic media. Report LBL-40504, UC-400, Lawrence Berkeley National Laboratory, Berkeley, CA.

[53] Yang IC, Rattray GW, Yu P. Interpretations of chemical and isotopic data from boreholes in the unsaturated-zone at Yucca Mountain, Nevada. US Geological Survey, Water-Resources Investigation Report-96-4058, Denver, CO, 1996.